UNIVERSITY OF CALIFORNIA
RIVERSIDE

Development and Application of Optical Coherence Elastography for Detection of Mechanical Property Changes Occurring in Early Osteoarthritis

A Dissertation submitted in partial satisfaction
of the requirements for the degree of

Doctor of Philosophy

in

Bioengineering

by

Koji Hirota

March 2017

Dissertation Committee:
Dr. B. Hyle Park, Chairperson
Dr. Jin Nam
Dr. William H. Grover

The Dissertation of Koji Hirota is approved:

_____

_____

_____

Committee Chairperson

University of California, Riverside

ABSTRACT OF THE DISSERTATION

Development and Application of Optical Coherence Elastography for Detection of Early Osteoarthritis

by

Koji Hirota

Doctor of Philosophy, Graduate Program in Bioengineering
University of California, Riverside, March 2017
Dr. B. Hyle Park, Chairperson

We demonstrate a computationally-efficient method for optical coherence elastography (OCE) based on fringe washout method for a spectral-domain OCT (SD-OCT) system. By sending short pulses of mechanical perturbation with ultrasound or shock wave during the image acquisition of alternating depth profiles, we can extract cross-sectional mechanical assessment of tissue in real-time. This was achieved through a simple comparison of the intensity in adjacent depth profiles acquired during the states of perturbation and non-perturbation in order to quantify the degree of induced fringe washout. Although the results indicate that our OCE technique based on the fringe washout effect is sensitive enough to detect mechanical property changes in biological samples, there is some loss of sensitivity in comparison to previous techniques in order to achieve computationally efficiency and minimum modification in both hardware and software in the OCT system. The tissue phantom study was carried with various agar

density samples to characterize our OCE technique. Young's modulus measurements were achieved with the atomic force microscopy (AFM) to correlate to our OCE assessment. Knee cartilage samples of monosodium iodoacetate (MIA) rat models were utilized to replicate cartilage damage of a human model. Our proposed OCE technique along with intensity and AFM measurements were applied to the MIA models to assess the damage. The results from both the phantom study and MIA model study demonstrated the strong capability to assess the changes in mechanical properties of the OCE technique. The correlation between the OCE measurements and the Young's modulus values demonstrated in the OCE data that the stiffer material had less magnitude of fringe washout effect. This result is attributed to the fringe washout effect caused by axial motion that the displacement of the scatterers in the stiffer samples in response to the external perturbation induces less fringe washout effect.

ACKNOWLEDGEMENTS

The dissertation, the research included herein and knowledge I have gain is a direct reflection of several individuals that have provided me with their support throughout my doctoral program. First and foremost, I would like to thank my advisor, Dr. B. Hyle Park for his dedicated guidance and support. He has fostered an environment of educational growth in his lab and afforded me the opportunity to be part of this environment. He provided valued key insight and vision throughout my overall project. I truly would have not been able to do it without him.

I would like to express my gratitude to my committee members, Dr, Jin Nam, and Dr. William H. Grover, for their mentorship. In the collaboration project, Dr. Nam provided me the continual guidance and insight to develop my knowledge base. Dr. Grover has provided warm and sincere supportive environment where I was able to bolster my confidence, he has always been very encouraging of my education pursuits.

I want to thank all of the members from the Neuroscience and Optical Imaging Research group at the University of California, Riverside. In particular, I would like to thank Christian Oh for his generosity and friendship over the years. He helped me so much to get through difficult times beyond much more than just work. I appreciate that he always stood by me in solid support. I like to thank Minh Tong and Monirul (Masum) Hasan for their friendship. I appreciated the solidarity between us at the lab and in the daily walks where we shared endless conversations. I wish them the best in the coming year as they complete their Ph.D's. I would also like to thank Jonathan Ma for helping through my Masters years and in his friendship after he completed his studies at UCR. I

want to thank Chris Hughes, Junze Liu, Andy Cho, Patrick Gregory, Jasmine Shah, and Danielle Ornelas for their support in the lab. I enjoyed their company and working with all of them. I wish them the all the best. I want to thank Dr. Yan Wang, Dr. Md. Shahidul Islam, Dr. Michael Oliveira, Dr. Md. Rezuanul Hague, Dr. Carissa Rodriguez, Dr. Melissa Eberle, and Dr. Yenisey Ponce de Leon for establishing and developing the lab. As it provided me with the opportunity to be part of it. I also want to thank Dr. Christopher Horner, Karen Low, Gerardo Ico, and Jenny Szu for the help they provided in completing my projects. I enjoyed interacting with them.

I also want to thank Kumar Thenkondar, Peter Hsieh, Masato Endo, Arthur Ortega, Dr. Karthik N. Thenkondar for their friendship and support throughout these years. I would like to thank Liliana Valle, Gabriela Valle, and Jose Luis Perez for their warm, generous and kind support and for treating me like family. I also want to acknowledge Toastmasters Club 290 for helping me improve my leadership and public speaking skills.

I would like to thank my father, Masukazu Hirota, and my mother, Hiroko Hirota, for their continued support in their endless encouragement and love. In particular, I would like to thank my father who encouraged me all the way from Japan via Skype to keep moving forward and who with his words of wisdom became my daily inspiration. To my mother who has strongly supported my educational growth, supported my father and family. To my grandmother, Ikuyo Hirota, who I still remember when I spoke to her the last time and I remember that she was kind and loving every day. To my grandfather, Masujiro Hirota, in his memory and who I still feel stands by me.

I would like to thank our family friends Rudy and Marilu Ceballos and the Ceballos family for their continued support. Anytime I needed help, they never hesitated to give me a hand and to treat me like a son.

I also like to thank Dr. Jacob Raifer, Dr. Ronald S. Swerdloff, Dr. Yanhe Lue, and Dr. Thomas Haider for collaboration work. I appreciated their feedback. I would like to acknowledge the funding source for the Department of Bioengineering at University of California, Riverside, Haider Biologics and NIH U01 EY025501 (AGI).

Table of Contents

Chapter 1: Background 1
Section 1.1: Optical coherence tomography (OCT) 1
Section 1.1.1: Principle of OCT 2
Section 1.1.2: Spectral-domain OCT 3
Section 1.1.2.1: Measuring optical power at spectrometer and wavelength assignment 8
Section 1.1.2.3: Fringe washout 9
Section 1.2: Osteoarthritis (OA) 10
Section 1.3: Function extensions of OCT 12
Section 1.3.1: Optical coherence elastography (OCE) 12
Section 1.3.2: Polarization-sensitive OCT (PS-OCT) 16
Section 1.3.3: Endoscopic OCT 16
Section 1.4: Conclusion 17
Chapter 2: OCT intensity imaging of testicle 18
Section 2.1: Introduction 18
Section 2.2: Identification of sperm from OCT images 21
Section 2.3: Comparison of heat-treated and normal 22
Section 2.4: Conclusion 24
Chapter 3: 1st approach to developing OCE 25
Section 3.1: Specification of OCT 25
Section 3.2: Fringe washout effect based OCE 26
Section 3.3: Speckle Noise 29
Section 3.4: Proof of concept – experimental methods 30
Section 3.4.1: Function generator driven ultrasound OCE apparatus 31
Section 3.4.2: Characterization of OCE with tissue phantom study 33
Section 3.4.3: Tissue phantom study with atomic force microscopy (AFM) 37
Section 3.5: *In vitro* study with arthritis induced rat cartilage 39
Section 3.5.1: Osteoarthritis induced rats model (MIA model) preparation 39
Section 3.5.2: *In vitro* study with OCE 40
Section 3.6: Conclusion 43

Chapter 4: 2nd approach to developing OCE 45
Section 4.1: Introduction to shock wave 45
Section 4.1.1: Shock wave OCE apparatus 46
Section 4.1.2: Characterization of OCE with tissue phantom study 47
Section 4.1.3: Tissue phantom study with AFM 53
Section 4.2: *In vitro* study with arthritis induced rat cartilage 55
Section 4.2.1: *In vitro* study with OCE 55
Section 4.2.2: *In vitro* study with AFM 57
Section 4.3 Conclusion 59
Chapter 5: Final approach to developing OCE 62
Section 5.1: Introduction to pulser-receiver driven ultrasound OCE 62
Section 5.1.1: Pulser-receiver driven ultrasound OCE apparatus 63
Section 5.1.1.1: Post-processing 65
Section 5.1.1.2: Ultrasound perturbation angle 67
Section 5.1.1.3: Ultrasound pulse timing 68
Section 5.1.2: Characterization of OCE with tissue phantom study 69
Section 5.1.3: Characterization of OCE with plastic samples 71
Section 5.1.4: Visualization of agar sphere 72
Section 5.2: *In vitro* study with arthritis induced rat cartilage with OCE 74
Section 5.3: Conclusion 76
Chapter 6: Conclusion and future studies 78
Section 6.1: Conclusion for OCE studies 78
Section 6.2: PS-OCT preliminary study 83
Section 6.3: Forward-viewing endoscope for arthroscopic OCT 86
Section 6.4: Side-viewing endoscope for arthroscopic OCT 94

List of Figures

Figure 1.1 Comparison of imaging depth and resolution between conventional imaging modalities to OCT [3]. 2

Figure 1.2 Schematic of Low coherence interferometry using Michelson interferometer . 3

Figure 1.3 Schematic of SD-OCT system. SLD: superluminescent diode, cir: circulator, spl: splitter, m: mirror, gm: galvanometer, gr: grating, lsc: CCD line scan camera 4

Figure 1.4 A depth profile (top left) represents the intensity as a function of depth. Scanning the optical beam across the sample creates a series of depth profiles that can be represented as a cross-sectional image (top right). Scanning a series of 2D images (bottom right) creates a 3D image (bottom left). Images are from testicular tubules imaging from Chapter 2. 5

Figure 1.5 Basic schematic of spectrometer used in SD-OCT (left). The detected spectrum at different depth (center) and corresponding depth profiles after Fourier transformation (right). 9

Figure 1.6 Intensity assessment of OA progressed cartilages with corresponding histology images. 13

Figure 2.1 (a) and (b) are cross-sectional intensity images of control and sperm reduced samples. (c) and (d) are cross-sectional attenuation images of both samples with sperm containing regions color-coded in yellow. (e) and (f) are the attenuation depth profile that attenuation as a function of depth. 22

Figure 2.2 (a) and (b) are the *en face* images of control and heat-treated samples respectively. (c), (d) and (e) are the histological images by using 200x magnification with stereomicroscope corresponding area (1), (2) and (3) respectively. 23

Figure 3.1 OCT intensity images with different averaging kernel size. No averaging filter was applied (top). 5x10 averaging filter was applied (middle). 10x20 averaging filter was applied (bottom). The optimal averaging filter was determined to be the middle image. 30

Figure 3.2 Function driven ultrasound perturbation power measured in an oscilloscope 31

Figure 3.3 Schematic of the OCE system employing function generator driven ultrasound perturbation system. sld: superluminescent diode (broadband light source), pc: polarization controller, pbs: polarization beam splitter, pm: electro-optic polarization modulator, c: fiber collimator, lsc: line scan camera. 32

Figure 3.4 Basic OCE post-processing and analysis 34

Figure 3.5 Different combination of OCT acquisition speed, ultrasound pulse frequency (kHz) and ultrasound amplitude parameter settings for OCE. Intensity difference was quantified for each setting. 36

Figure 3.6 Calculated intensity difference in dB at difference amplitude of ultrasound pulse for difference agar density (%) 37

Figure 3.7 (a) Calculated intensity difference (dB) for each agar density. (b) Measured Young's modulus value for each agar density. (c) intensity difference for each agar density compared to measured Young's modulus for each agar density. 38

Figure 3.8 Schematic of the OCE system with a MIA model knee sample in place. The OCE imaging direction (scanning direction) and ultrasound perturbation direction are shown. 41

Figure 3.9 The red box indicates the region in cartilage where the intensity difference was calculated. The area is just below the tide mark. 41

Figure 3.10 Calculated intensity difference (dB) for each MIA model. 42

Figure 4.1 Schematic for the OCE system employing shock wave perturbation. 47

Figure 4.2 (a) an OCT intensity image capturing a shock wave pulse with in a cross-sectional frame. (b) a plot of the average intensity value of the agar layer over 2048 depth profile points. 49

Figure 4.3 The construction of fringe washout induced OCT intensity image in empty array. 50

Figure 4.4 (a) An OCT intensity image frame without shock wave perturbation. (b) An OCT intensity image frame capturing a shock wave pulse. (c) A fringe washout induced OCT intensity image frame. (d) An OCE image frame of calculated intensity difference 51

Figure 4.5 Calculated intensity difference in dB scale for each agar density sample. 52

Figure 4.6 (a) Calculated intensity difference for each agar density sample. (b) Measured Young's modulus values over difference agar density samples. (c) Calculated intensity difference for each agar density compared to measured Young's modulus for each agar density. 54

Figure 4.7 Schematic of the OCE system with a MIA model knee sample in place. The OCE imaging direction (scanning direction) and ultrasound perturbation direction are shown. 56

Figure 4.8 (a) (b) (c) (d) the OCT intensity images of MIA-day 0, MIA-day 3, MIA-day 5 and MIA-day 11. (e) (f) (g) (h) corresponding OCE images. 56

Figure 4.9 (a) Depth-dependent changes of intensity difference analyzed from OCE imaging, and (b) Young's modulus measured by AFM of control vs. MIA-day 11 damaged cartilage, showing similar trends that indicative of cartilage stiffening due to MIA. (c) OCE depth imaging limitation. 58

Figure 5.1 Comparison of perturbation power of ultrasound driven by a function generator and ultrasound driven by a pulser-receiver with the same transducer. 64

Figure 5.2 (a) Schematic of the OCE system with synchronized ultrasound perturbation system. (b) Trigger synchronization of OCE system. 65

Figure 5.3 Post-processing of OCE data with depth profile separation, speckle reduction and area comparison 66

Figure 5.4 (a) Ultrasound perturbation angle α and the scanning direction. (d) difference perturbation angle α to scanning direction. 67

Figure 5.5 Calculated intensity difference for each probe angle (perturbation angle) α. . 68

Figure 5.6 (a) pulse delay time Δt. (b) The distance between ultrasound probe and a sample set to 40 mm. (c) Calculated intensity difference for each Δt. 69

Figure 5.7 (a) OCE image of an agar sample. (b) Calculated intensity difference for each sample. (c) Measured Young's modulus for each sample. (d) Calculated intensity difference for each sample compared to measured Young's modulus for each agar density 71

Figure 5.8 The OCT intensity cross-sectional image of the agar sphere. (b) The OCE cross-sectional image of the agar sphere. (c) The OCE cross-sectional image of the agar sphere shown in the OCT intensity volumetric image. (d) The OCE volumetric image with the OCE image frames shown above. 73

Figure 5.9 (a – 1) (a –2) (a – 3) the OCE cross-sectional images of the OCE volumetric image at the different locations for MIA-day 0 knee sample. (b – 1) (b – 2) (b – 3) the OCE cross-sectional images of the OCE volumetric image at the different locations for MIA-day 11 knee sample. 75

Figure 5.10 Average intensity difference as a function of depth for an cross-sectional image. 76

Figure 6.1 Schematic of PS-OCT system 84

Figure 6.2 PS-OCT images of MIA model cartilages and corresponding phase retardation as a function of depth 85

Figure 6.3 OCE (left) and PS-OCT (right) images of cartilage under a thin layer of chicken muscle. The border between the two different tissues is indicated by the triangles. 86

Figure 6.4 Schematic of first prototype of forward-viewing endoscope and a picture of built prototype. 89

Figure 6.5 Schematic of piezoelectric bending actuators. 91

Figure 6.6 (a) schematic of an endoscope with MEMS mirror. (b) the recent prototype of the endoscope. 92

Figure 6.7 OCT endoscope (arthroscope) insertion into osteoarthritis induced rat cartilage in in vivo study 95

Figure 6.8 Schematic of side-viewing endoscope probe 95

List of Acronyms

OCT: optical coherence tomography

MRI: magnetic resonance imaging

SD-OCT: spectral domain optical coherence tomography

SLD: superluminescent diodes

GPU: graphic processing unit

CCD: charge-coupled device

OA: osteoarthritis

ECM: extracellular matrix

GAG: glycosaminoglycan

dGEMRIC: delayed assessment of gadolinium-enhanced magnetic resonance imaging of cartilage

OCE: optical coherence elastography

SNR: signal to noise ratio

AFM: atomic force microscopy

MIA: monosodium iodoacetate

IACUC: Institutional Animal Care and Use Committee

DAQ: data acquisition

PS-OCT: polarization sensitive optical coherence tomography

FNA: fine needle aspiration

PARS: paired-angle-rotation scanning

GRIN: gradient-index

MEMS: microelectromechanical system

NOA: non-obstructive azoospermia

ICSI: intracytoplasmic sperm injection

IVF: *in vitro* fertilization

cTESE: conventional testicular sperm extraction

Micro-TESE: microdissection testicular sperm extraction

SRR: sperm retrieval rate

Chapter 1: Background

Section 1.1: Optical coherence tomography (OCT)

Optical coherence tomography (OCT) is a promising technique for clinical imaging that is capable of minimal-invasive, high-resolution, and label-free imaging. OCT is a label-free optical imaging modality that allows for visualization of microscopic structures in biological tissue with inherent contrast. OCT was recently used in many clinical and research contexts [1]. OCT is capable of producing cross-sectional images, and volumetric images of biological tissue in real time by raster scanning. With use of galvanometers, OCT can form geometrically similar histology images. OCT can achieve penetration depths of 1-3mm in scattering media, including biological tissue with 1-10μm axial resolution and ~20μm lateral resolution with a scanning range of 10mm by 10mm area. This combination of high resolution and penetration depth allows OCT to occupy a niche between more traditional optical imaging methods, including confocal microscopy and medical imaging techniques such as ultrasound, magnetic resonance imaging (MRI) involving depth penetration and spatial resolution. OCT imaging technique has found its application in the field of cardiology, gastroenterology pulmonology, ophthalmology, dermatology and neuroscience [2].

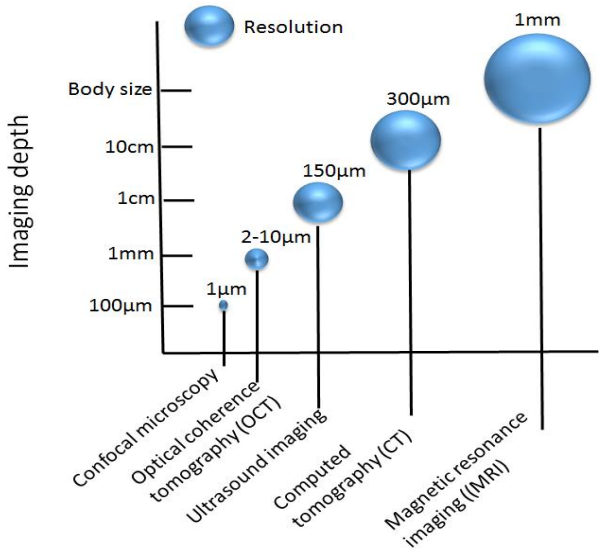

Figure 1.1 Comparison of imaging depth and resolution between conventional imaging modalities to OCT [3].

Section 1.1.1: Principle of OCT

The basic principle of OCT is analogous to ultrasonic imaging. OCT has an ability to create depth resolved structural images of a biological sample by sending sound pulses into the sample and a detector measures the amplitude and time delay of reflected sound pulses sent back from the sample. OCT acquires depth-resolved imaging in the same manner by using light rather than sound. Since light travels so much faster than sound in a media, the time delay cannot be directly measured but using low coherence interferometry. With low coherence interferometry, the magnitude and echo-time delay of light can be measured by comparing light scattered from a sample and light reflected back from a reference.

Section 1.1.2: Spectral-domain OCT

A typical OCT system is implemented with a low coherence interferometry which consists of a Michelson interferometer and a low coherence light source. The low coherence interferometry is commonly built with a sample arm, a reference arm, a detector and a low coherence light source shown in Figure 1.2. Light from the source is split to sample and reference arms with an optical splitter. The backscattered light from the sample and the reflected light from the reference arm recombine and are sent to the detector through an optical circulator. The depth-resolved information of the sample is formed by the interference of recombining the light from both arms. In order to obtain the precise depth-resolved image, the low coherence light source can be utilized to create constructive interference if the path length mismatch between the sample and reference arms is within the coherence length of the light source.

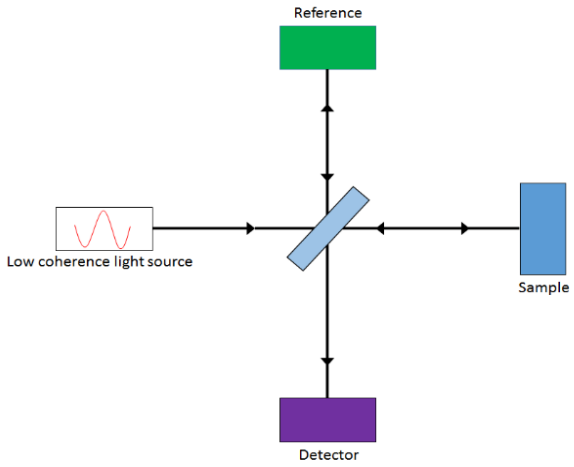

Figure 1.2 Schematic of Low coherence interferometry using Michelson interferometer.

OCT systems are comprised of a light source, a reference arm, a sample arm and a detection arm commonly found in interferometry setups. Second generation OCT systems

were Fourier-domain systems in which the reference arm remained stationary and the interference was detected as a function of wavenumber using a spectrometer (spectral domain) [4, 5]. The interfered light in the detection arm is distributed by a grating and detected in a spectrally resolved manner on a line scan camera. The current setup of our OCT system is the single mode fiber-based spectral-domain OCT (SD-OCT) system. Figure 1.3 shows the schematic of the OCT system.

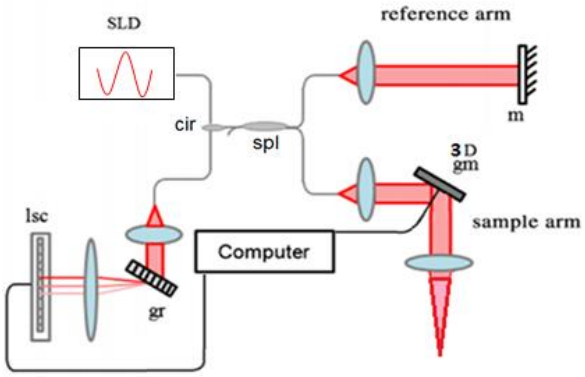

Figure 1.3 Schematic of SD-OCT system with SLD: superluminescent diode, cir: circulator, spl: splitter, m: mirror, gm: galvanometer, gr: grating, lsc: CCD line scan camera [6].

The broadband light source is sent into a circulator through a splitter to split the light between the sample arm and the reference arm. The reflected light from both arms recombined at the splitter. The interfered light is redirected by the circulator to the detection arm. At the detection arm, the light is collimated, dispersed by a grating and focused onto a line scan camera. Galvanometer mounted mirrors in the sample arm are controlled by the image acquisition program to achieve raster scanning. The measured intensity as a function of depth provides a depth profile, also known as A-line. A two-dimensional (2D) cross-sectional image is formed by acquiring sequential depth-profiles

across the sample in a given direction. The taking of consecutive cross-sectional images at the different lateral positions forms three-dimensional (3D) image of the sample.

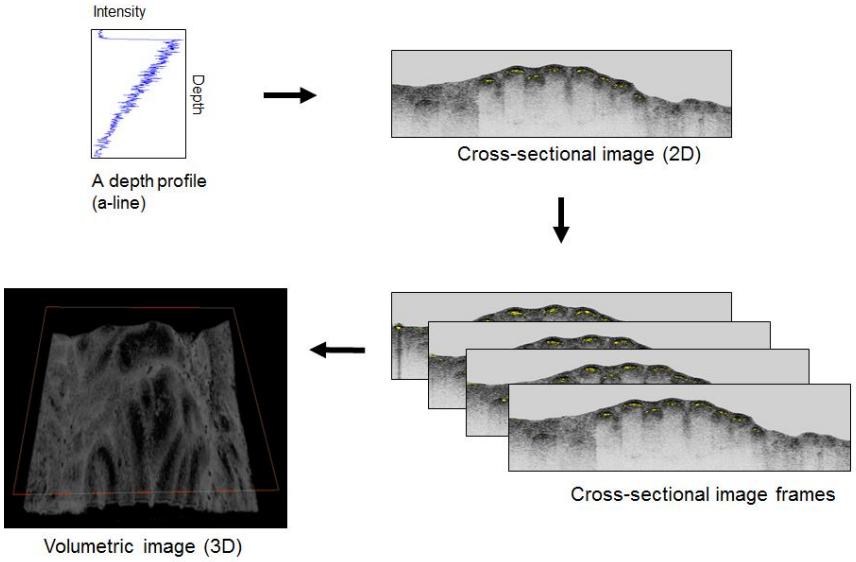

Figure 1.4 A depth profile (top left). Multiple depth profiles to create a cross-sectional image (top right). Multiple cross-sectional images (bottom right) create a 3D image (bottom left). Images are from testicular tubules imaging project in Chapter 2.

The following is the convention by Izatt and Choma [7] to measure the OCT intensity with low coherence interferometry. They considered that an interferometer is illuminated by a polychromatic plane wave where a complex electric field can be expressed as shown in Equation 1.1.

$$E_{src} = s(k,\omega)e^{(i[kz-\omega t])} \qquad \text{(Eq.1.1)}$$

k is the wavenumber ($2\pi/\lambda$), ω is the angular frequency ($2\pi\nu$), z is the optical path length along the propagation direction, t is the time, $s(k,\omega)$ is the amplitude of the electric field and $e^{(i[kz-\omega t])}$ is the complex phase that is as a function of spatial and temporal frequencies. The incident wave is split equally between the sample arm and reference

arm, the electric field at the reference and sample arms can be described as Equation 1.2 and 1.3.

$$E_R = \frac{s(k,\omega)}{\sqrt{2}}\sqrt{R_r}e^{[i(2kz_r-\omega t)]} \quad \text{(Eq. 1.2)}$$

$$E_S = \frac{s(k,\omega)}{\sqrt{2}}\sqrt{R_s}e^{[i(2kz_s-\omega t)]} \quad \text{(Eq. 1.3)}$$

Equation 1.2 and 1.3 assume that a single reflector is placed in each arm having reflectance of R_r and $R_s$at optical length of z_r and z_s. The factor of two in equation 1.2 and 1.3 is considering the optical pathlength of the round trip to the reflector and back. A more realistic electric field expression for the sample arm can be written as shown in Equation 1.4.

$$E_S = \frac{s(k,\omega)}{\sqrt{2}}\sum_{n=1}^{N}\sqrt{R_s}e^{[i(2kz_{s_n}-\omega t)]} \quad \text{(Eq. 1.4)}$$

Since biological samples are considered to have a series of reflectors at various depths within its sample, the equation 1.4 takes the sum of reflectors into consideration to the total detected signal. As mentioned previously, light reflected back from the reference and sample arms interfere and detect in the low coherence interferometry. The intensity at the detector can be expressed as shown in Equation 1.5.

$$I_D(k,\omega) = \frac{\rho}{2}\langle E_R + E_S\rangle^2 \quad \text{(Eq. 1.5)}$$

where ρ is the detector sensitivity, E_R and E_S are the electric field from the reference arm and sample arm respectively and the angular brackets denote integration over response time of the detector. The equation 1.5 that expresses the intensity at the detector

consisting of sample and reference arms is now written as Equation 1.6 by substituting Equation 1.2 and 1.4 into Equation 1.5,

$$I_D(k) = \frac{\rho}{4} S(k)^2 [R_r + \sum_{n=1}^{N} 2\sqrt{R_r R_s} \cos\big(2k(z_r - z_s)\big) + \sum_{n=1}^{N} \sum_{m=1}^{N} \sqrt{R_{s_n} R_{s_m}} e^{[i2k(z_r - z_{s_n})]} e^{[-i2k(z_r - z_{s_n})]}] \quad \text{(Eq. 1.6)}$$

The first term is an offset. The second term describes the depth information of the sample where the amplitude of the backscattered light is proportional to a_s and the frequency of the cosine provides the axial position. The last term includes autocorrelation information of the interference between all the reflectors from the sample and is only observed near z = 0 [8, 9]. The intensity as a function of depth is achieved by performing a Fourier transformation of the interference signal at the detector [4, 8, 10].

$$FT^{-1}[I_D(k)] = \frac{\rho}{8}\big[\gamma(z)\big(R_r + R_{s_1} + R_{s_2} + \cdots\big)\big] + \frac{\rho}{4}[\gamma(z) \otimes \sum_{n=1}^{N} \sqrt{R_r R_s}\,\delta(z \pm 2\big(z_r - z_{s_n}\big))] + \frac{\rho}{8}[\gamma(z) \otimes \sum_{n \neq m=1}^{N} \sqrt{R_{s_n} R_{s_m}}\,\delta\left(z \pm 2\big(z_{s_n} - z_{s_m}\big)\right)] \quad \text{(Eq. 1.7)}$$

$\gamma(z)$ represents the Fourier transformation of the power spectral dependence term $s(k,\omega)^2$ and $\otimes$ denotes convolution. From Equation 1.7, the specific optical path length mismatches between the refence and sample reflectors results in specific output frequencies at the spectrometer. The biological sample usually contains multiple reflectors in depth. The spectral interferogram is modulated with multiple cosines, each

frequency and amplitude correspond to the optical path length mismatch between a given sample reflector and the reference reflector .

Section 1.1.2.1: Measuring optical power at spectrometer and wavelength assignment

OCT uses a spectrometer as a detector to acquire depth resolved profiles known as depth profiles. The axial resolution and imaging depth sensitivity of SD-OCT can be determined by the design of the spectrometer. The typical components of a spectrometer include the grating, focusing lens, and charge-coupled device (CCD) camera used to measure the spectrum of detected light in the SD-OCT. When the constructive interference of reflected light from sample and reference comes back to the spectrometer, the grating distributes the light on to CCD line scan camera pixels according to wavelength. CCD pixel array then measures the interference fringe as a function of wavenumber k, which is expressed as $k = 2\pi/\lambda$ where λ is the optical wavelength. The spectrometer measures the axial position of the reflector in the sample arm by the frequency of the modulation on the detected spectrum. Low frequency modulations correspond to shallow reflectors while high frequency modulations correspond to deep reflectors in a sample. The signal strength in the depth is determined from the fringe amplitude in wavenumber. Performing a Fourier transformation on the spectral intensity function in the k domain to the x domain creates a depth profile that is intensity as a function of depth. Figure 1.5 shows the basic schematic of spectrometer used in SD-OCT.

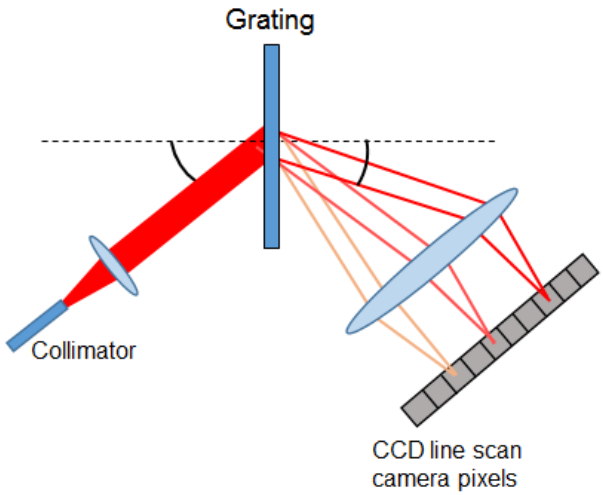

Figure 1.5 Basic schematic of spectrometer used in SD-OCT (left). The detected spectrum at different depth (center) and corresponding depth profiles after Fourier transformation (right).

This requires the data to be evenly sampled in *k*-space. This data acquisition requires each wavelength of interfered light to be assigned to the designated pixel on CCD line scan camera. The correct wavelength assignment can be achieved through approximate assignment of wavelength to each pixel by grating equation in the hardware and then applying calibration correction in the software. Each wavelength is converted to a wavenumber and then resampled at regular intervals in *k*-space by using interpolation, prior to the Fourier transformation.

Section 1.1.2.3: Fringe washout

Spectral interference fringe is measured in the spatial domain by means of a diffraction grating and a charge-coupled device (CCD) array. Individual pixels of the CCD array measure the optical power as a function of wave number $k = 2\pi/\lambda$ where λ is the optical wavelength. The output voltage of each CCD pixel is proportional to the number of

photon-generated electrons accumulated during an exposure time, T of the CCD [11]. The depth profile acquisition time *T* becomes equal to the depth profile period if the CCD is operated. Axial motion occurring during the acquisition of an OCT depth profile is known to cause fringe washout, in which the integrated spectral modulations on the spectrometer are dampened [11]. Previous researches have been focused on minimizing the effect to reduce motion artifacts during OCT acquisition [12, 13] by minimizing exposure time during acquisition of an individual depth profile. Our OCE method exploits this effect to determine the cartilage damage correlation to reduction in reflected intensity as well as being computationally-efficient.

Section 1.2: Osteoarthritis (OA)

The main focus on this dissertation is the development and application of OCT for detecting osteoarthritis (OA) at early stage. Osteoarthritis (OA) is one of the most common diseases afflicting major populations [14, 15]. The prevalence of OA is caused by stress on joints resulting in damages to cartilage. However, the main reason for the increase prevalence of OA is to the symptoms of aging and obesity [16]. The clinical therapy available for OA is limited, there are currently no surgical or pharmaceutical interventions available to fully restore damaged [14, 15]. The lack of full restoration of OA is largely attributed to the ability of detecting the disease before the condition of the cartilage reaches the irreparable cartilage damage condition and an avascular nature where cartilage has a very limited self-regenerative capability to restore cellular and extracellular matrix (ECM) damage. However, the study from *in vitro* and animal model

suggests that during the initial period of damage cartilage cell can be functionally restored to prevent further cartilage degeneration with the use of proper therapy [17]. In order to take advantage of this therapeutic window of opportunity, the early detection of OA is crucial. Current clinical standard for diagnosis of traumatic joint injury relies on low-resolution imaging technique or arthroscopic visual inspection of cartilage surface morphology. Many modalities focus on the elastic properties of tissue as a contrasting mechanism to assess and diagnose cartilage damage. Although the standard imaging modality for the assessment of cartilage damage involves the observation of superficial morphology by traditional X-ray radiography, this technique utility is limited by the poor sensitivity and a relatively large precision error results that can be achieved. Magnetic resonance imaging (MRI) based techniques are utilized to examine changes in cartilage volume and thickness [18] and semi-quantitative grading of an entire knee from MRI images [19, 20]. However, the notable changes in cartilage volume, thickness or any other remarks appear in the late-stage OA. The traditional MRI methods are unable to reliably detect the subsurface damages or changes associated in proteoglycans. Proteoglycans are known proteins in cartilage, water contents and collagen disorganization [21]. T2 and T1rho mapping in MRI are sensitive to detect tissue hydration and collagen organization that can assess degenerated cartilage based on its hydration and organization level [22, 23]. However, degradation in tissue hydration and collagen organization appears in a cartilage during mild-stage OA [24]. Delayed assessment of gadolinium-enhanced magnetic resonance imaging of cartilage (dGEMRIC) is capable of visualizing glycosaminoglycan (GAG) content, which chains

of GAG make proteoglycans, during the OA progression [25-27]. The deterioration of GAG content in cartilage is one of the early changes observed at initial stages of OA [28, 29]; therefore, the technologies that can find the small mechanical property changes and compare it to the normal state of cartilage would lead to the early-stage detection of OA. In order to take advantage of this therapeutic window, our goal is to develop a non-destructive, high-resolution and label-free combination of optical coherence tomography (OCT) [1] based methods for early detection of OA.

Section 1.3: Function extensions of OCT

In addition to the depth-resolved intensity information of in biological tissue, OCT can provide other information about the sample with inherent contrast such as optical coherence elastography (OCE) and polarization-sensitive OCT (PS-OCT) for birefringence. As imaging depth is limited in OCT, systems can be modified in both hardware and software to allow the sample arm to have an endoscopic feature. The OCE, PS-OCT and endoscope are not the only extensions of OCT function; however, this dissertation focuses mainly to these extensions for assessment of OA.

Section 1.3.1: Optical coherence elastography (OCE)

Measuring intensity by OCT can quantitatively assess the mechanical property changes in OA progressed cartilages. An average intensity as a function of subsurface depth was determined by laterally averaging the linear intensity as a function of depth. Intensity changes of cartilages as OA progress should be evident by comparing the intensity depth

section of the tidemark between cartilage and bone. Figure 1.6 is an example of the intensity assessment of OA cartilage. The blue dotted region depicts intensity depth profiles founded in the cartilage and the orange dotted region depicts the bone. The tidemark region is indicated between second blue dot line and first orange dot line from left in intensity depth profile plots. The depth of the tidemark can be seen to be decreasing as OA progresses.

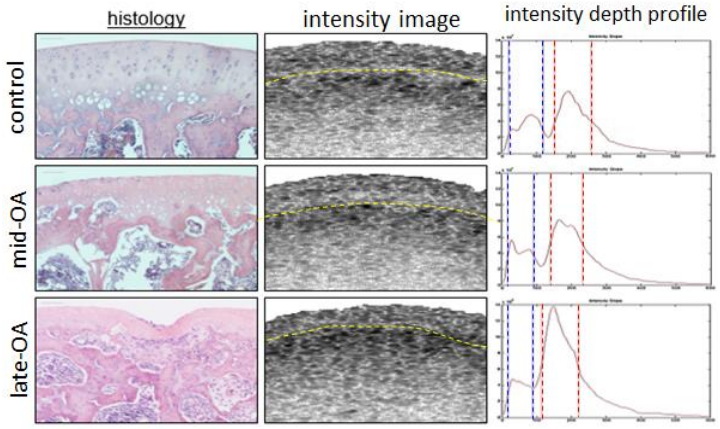

Figure 1.6 Intensity assessment of OA progressed cartilages with corresponding histology images.

Although the OCT intensity analysis of biological tissue can provide meaningful information of small mechanical property defects in biological tissue, identifying the small defects is difficult to be visualized with intensity. Intensity analysis is also computationally intensive where the use of another type of inherent contrast is needed to detect the mechanical property changes of biological tissue. The extension of OCT technique is not limited to its own functions. The OCT can be used to interfere with other external devices due to its feasibility. Elastography is a medical imaging modality that maps the local mechanical properties of tissue changes by the progression of disease such

as arthritis. It uses medical imaging to measure the deformation in response to mechanical loading. Elastography gives elastograms images which provides insight into the progression of disease [30]. Elastography was largely developed around ultrasound and magnetic resonance imaging techniques that are capable of diagnosing tumor cells in the breast, liver and pancreas [31].

OCT has been used in the field of elastography since 1998 as known as optical coherence elastography (OCE). OCT was introduced to the field of elastography and offers distinct features compared to ultrasound elastography and magnetic resonance elastgraphy where OCT provides non-destructive, high-resolution and label-free combination imaging. Jacques *et al* and Schimitt first introduced optical elastography technique employing OCT to detect depth-revolved sample deformation. Optical coherence elastography (OCE) offers a distinct higher spatial resolution and higher magnitude feature compared to ultrasound and magnetic resonance elastography [30, 32-34]. Also, OCE provides a three-dimensional imaging capability in millimeter-scale imaging depth, unlike the atomic force microscopy limited to its field of view and the specific measurement procedure [34].

Previous OCE utilized speckle tracking, phase-sensitive detection and Doppler spectrum detection techniques to quantify the mechanical property changes in biological tissue. Each technique measures the displacement and deformation of the sample tissue resulted from external or internal compressive loading. Speckle tracking takes the advantages of speckle realization which require speckle patterns of specific scatterers in order to determine the precise location of the scatterers within the tissue samples.

Measuring the speckle pattern shift in the displacement of the scatterers during the mechanical loading can estimate the strain of the tissue in the resulting speckle decorrelation. The advantage of this technique is its capability of tracking the speckle in more than one spatial dimension. The major limitation of this technique is the minimal measurable displacement [30].

Unlike the speckle tracking technique, the phase-sensitive detection technique has much higher displacement range. This technique allows access to the phase of the detected signal by phase unwrapping. However, this phase unwrapping invalidates the assumption of the linear relationship between the phase difference and displacement. Furthermore, the phase unwrapping is easily affected by the single-to-noise ratio (SNR) [30].

Doppler spectrum detection was introduced to overcome the limitation of low SNR adaption in the phase-sensitivity detection. Doppler spectrum detection was achieved by combining spectral and time-domain OCT, and applying the Fourier transform and a second Fourier transform in the time domain. The downsides of this technique are high volume of acquired data and is computationally intensive that makes it impractical and difficult to implement in real time visualization. In this thesis, OCE is considered as a type of OCT's inherent contrast that is used to analyze mechanical property changes of biological tissue.

Section 1.3.2: Polarization-sensitive OCT (PS-OCT)

Another mode of inherent contrast that OCT can provide is measuring the birefringence of biological tissue. Birefringence is the optical property of a material having a refractive index that depends on the polarization state and propagation direction of light. Highly organized biological tissues such as fibrous muscle, tendon, myelin sheath of nerve axons, and fatty tissue have this birefringent feature. To measure birefringence with OCT, the incident light must be sent through a polarization modulator to alternate the light between two orthogonal polarization states between adjacent A-lines. Also, the spectrometer must also be modified to have a polarizing beam splitter and an additional CCD line scan camera to detect the orthogonal polarization states separately. This OCT system with polarization function is known as polarization-sensitive OCT (PS-OCT). The calculation of phase retardation between two orthogonal polarization states and the image assembly are explained in detailed in Chapter 6.

Section 1.3.3: Endoscopic OCT

Although OCT fills the gap between more traditional optical imaging methods such as confocal microscopy and medical imaging techniques such as ultrasound and magnetic resonance imaging, the imaging penetration depth of OCT is limited to a few millimeters. OCT can not visualize biological structures located deeper in the tissue. The only way to gain access is to surgically expose the target regions. This limitation can be overcome by implementing endoscopic sample arms where needle-like endoscopes can be inserted into

the local area in a minimally invasive manner. This endoscopic OCT technology is explained in depth in Chapter 6.

Section 1.4: Conclusion

A smaller number of separate studies have been conducted to investigated the use of OCE [35] to examine the overall mechanical properties of cartilage [36]. The previous OCE methods are very sensitive and accurate to measure mechanical property changes in biological tissues. However, these methods are also very computationally-intensive, and these methods do not provide three-dimensional imaging. Our goal is to develop an OCE method that takes advantage of an imaging artifact, fringe washout effect [11]. Although, this fringe washout method is a less sensitive OCE method compared to previous methods, it is sufficient enough to detect the mechanical property changes in cartilage tissue at the early-stage OA [37]. Our OCE method is practical to implement to existing OCT system to acquire volumetric imaging with minimal system modification and in a computationally-efficient manner.

Chapter 2: OCT intensity imaging of testicle

Section 2.1: Introduction

The primary function of OCT is imaging subsurface structures of biological tissues without exogenous labels. OCT uses inherent contrast such as intensity and attenuation that can be calculated from OCT data obtained. This inherent contrast can be color-coded to enhance hidden biological structures that may be hard to see from typical OCT images. In Chapter 2, we demonstrate the possible solution to definitively identify seminiferous tubules containing sperm without removing testicular tissue with use of OCT inherent contrast. This work has been in collaboration with Dr. Jacob Rajfer, M.D. and Dr. Ronald S. Swerdloff from University of California, Los Angeles (UCLA), Harbor-UCLA Medical Center, and Dr. YanHe Lue from LA BioMed.

About 15% of married couples encounter fertility issues, with 40% of that number caused by male infertility. Azoospermia, which defines as the absence of spermatozoa in the ejaculate, is observed approximately in 1% of the population and 15% of infertile men. Among patients with azoospermia, about 40% are caused by post-testicular obstruction that can be corrected by surgical procedures [38]. The remaining 60% of azoospermia are non-obstructive azoospermia (NOA) caused by congenital or acquired spermatogenetic defects. NOA is the most severe and difficult to treat form of male infertility.

Before advances in assistive reproductive technology, the options for treating patients with NOA were minimal and limited to donor insemination. The invention of intracytoplasmic sperm injection (ICSI) now provides an opportunity for patients with

NOA to father children using surgically-retrieved sperm from their own testes for *in vitro* fertilization (IVF). Multiple surgical procedures have been developed and used clinically to retrieve sperm from seminiferous tubules of patients with NOA, which include fine needle aspiration (FNA), open testicular biopsy or conventional testicular sperm extraction (cTESE), and microdissection testicular sperm extraction (micro-TESE). FNA is a percutaneous testis biopsy technique. It is simple and minimal invasive, but its sperm retrieval rate (SRR) is lower than cTESE. cTESE is a surgical procedure during which random incisions in the tunica are made and a variable volume of testicular parenchyma are removed for sperm *in vitro* retrieval. These multiple random tunica incisions or large resection of parenthyma during cTESE may result in testicular devascularization and atrophy that may cause damage on the residual spermatogenesis and hormone production after surgery [39].

Micro-TESE has been developed as an advantageous and optimal technique for sperm extraction [38]. It is minimally invasive, safe, and limits the disruption of testicular function. The SRR obtained using micro-TESE is higher than that of CTESE in NOA men. With the guidance of an operating microscope during testicular exploration, the testicular blood supply is visualized and preserved. The seminiferous tubules that are most likely to contain spermatozoa are identified and specifically targeted for extraction and sperm retrieval. Micro-TESE has a lower complication rate when compared with other testicular sperm retrieval procedures. However, micro-TESE requires a significant learning curve and long operative times depending on how long it takes to find seminiferous tubules containing sperm.

The major technical challenge with micro-TESE has been the inability to definitively identify seminiferous tubules that contain sperm without removing testicular tissue. After surgically opening the tunica albugenia and exposing the testicular parenthyma, the decision where to excise a portion of seminiferous tubule is subjective, and totally dependent on the surgeon's experience in visually identifying the appearance of larger and more opague tubules more likely to contain sperm. With this technique, experienced surgeons, who have conducted more than 50 cases of micro-TESE procedures, have achieved an SRR of nearly 50% depending on the underlying cause of azoospermia [40].

OCT is an attractive potential solution to the guesswork involved in micro-TESE since OCT can image tissue microstructure without exogenous labels up to 2mm below the surface of tissue with micron-level resolution. Although OCT is a potential system to give guidance to micro-TESE procedure, there have been only limited studies using OCT as a method for improving SRR in TESE procedures [41, 42]. The application of operating microscope with integrated OCT guidance to the region of seminiferous tubules containing spermatozoa will shorten the surgeon's learning curve and make the micro-TESE procedure more feasible and practical for surgeons to treat patients with NOA. This approach is expected to increase the sperm retrieval rate in future clinical application.

Section 2.2: Identification of sperm from OCT images

We have achieved preliminary studies through our OCT system. Testes used for the initial studies were atrophic testes from Sprague-Dawley rats treated with testicular hyperthermia. In LA BioMed, We have previously demonstrated that nine days after testicular hyperthermia (immersing testes in 43^{o} water bath for 15 min) the majority of spermatocytes and round spermatids were depleted while the spermatozoa at stage VII and VIII remained in the seminiferous tubules [43, 44]. Under anesthesia, the scrota containing testes were immersed into water bath at 43^{o} for 15 minutes. After nine days, testicular hyperthermia heat-treated and control rats were sacrificed with an overdose of intraperitoneal injection of sodium pentobarbital. An incision was made on the scrotum and the testes were taken out and put into cold PBS. After placing testis on a petri dish, the unica albuginea was cut open to expose the seminiferous tubules. The testicular parenchyma was imaged by OCT.

OCT acquired volumetric data. OCT scanned 2mm by 4mm lateral area with 200 frames, each frame composed of 2048 depth profiles with a 2mm depth. Figure 2.1 shows the selected cross-sectional images from volumes acquired from a control and heat-treated animal. Figure 2.1 (a) and (b) depict the intensity images with increased backscattered intensity shown in darker colors. Sperm can be seen in these intensity images as pockets of increased intensity inside of seminiferous tubules corresponding to sperm in the control sample and much less in the treated one. However, automated segmentation and identification of these regions from only intensity information is computationally intensive, and difficult to implement in real times. Applying a recently

published algorithm to compute depth-revolved attenuation [45] yields Figure 2.1 (c) and (d) where simple thresholds for regions with higher attenuation ($\mu > 5$) which allows for rapid and computationally-efficient detection of sperm (shown in yellow for mild attenuation and red for high attenuation). The difference in attenuation level indicated by red and yellow colors is the sperm counts that the region in red color contains more sperm than the region in yellow does. The depth profiles shown in Figure 2.1 (e) and (f) are of the average attenuation in the region indicated between the redlines. In Figure 2.1 (c) and (d) include increased attenuation indicating the location of sperm.

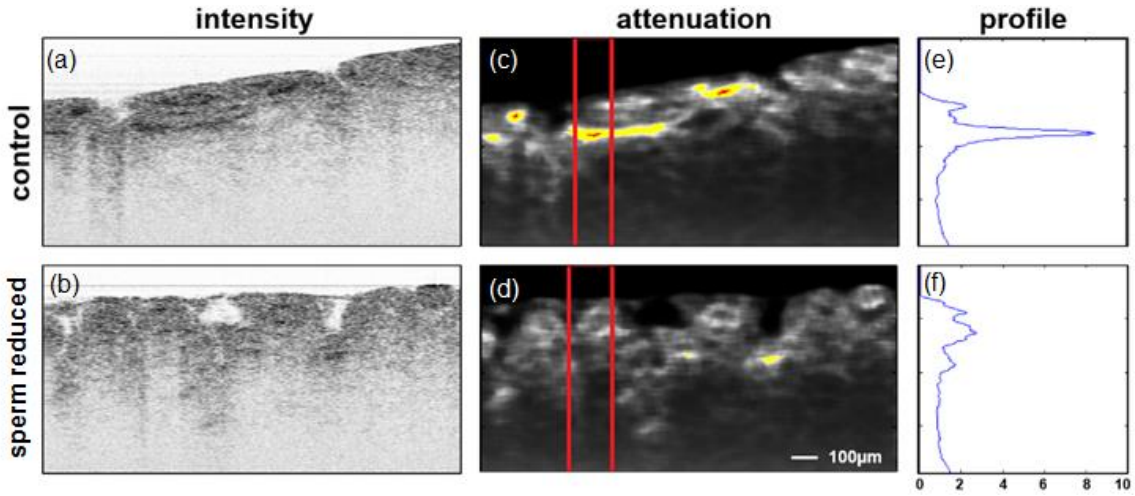

Figure 2.1 (a) and (b) are cross-sectional intensity images of control and sperm reduced samples. (c) and (d) are cross-sectional attenuation images of both samples with sperm containing regions color-coded in yellow. (e) and (f) are the attenuation depth profile that attenuation as a function of depth.

Section 2.3: Comparison of heat-treated and normal

Top down visualization of the region of interest can be facilitated by *en face* reconstruction of the highlighted regions in all frames of an acquired volume in Figure 2.2 (a) and (b). The *en face* image without visualizing details of tubules was generated

based on the surgeons' preference that the image can visualize the scanned area at once to indicate the sperm containing location. Figure 2.2 (a) shows 4mm by 2mm scanned area with 200 frames for each frame composed of 2048 depth profiles. The *en face* image shows the sperm region up to 2mm in depth where all the color-coded area was added together. Sections of tubules from regions of interest identified from these reconstructions were extracted and interior of the tubules was imaged at 200x magnification with a stereomicroscope. Figure 2.2 (c), (d) and (c) are the corresponding 200x magnification images of area (1), (2) and (3) respectively. The concentrated color-coded area in yellow indicates the area where the concentration of sperm count exists in area (2) and Figure 2.2 (d) was the evidence of this confirmation. The presence or absence of sperm from tubules with elevated or normal levels of attenuation provide preliminary confirmation that hidden sperm can be detected using OCT.

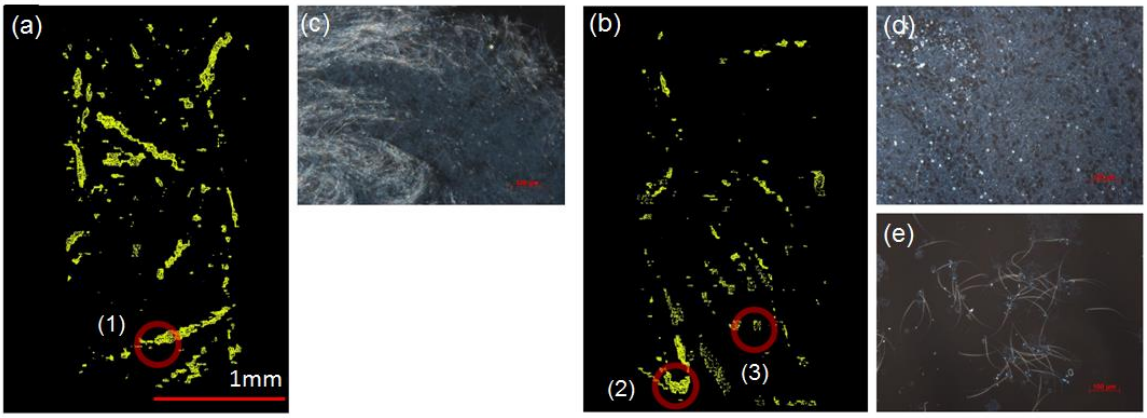

Figure 2.2 (a) and (b) are the *en face* images of control and heat-treated samples respectively. (c), (d) and (e) are the histological images by using 200x magnification with stereomicroscope corresponding area (1), (2) and (3) respectively.

Section 2.4: Conclusion

This project was to examine the use of OCT's primary function that is able to image subsurface structure of biological tissue with its inherent contrast in intensity and attenuation. Based on these calculated inherent contrasts, OCT images can provide the ability to color-code the region of distinguished features in sperm. In this project, this inherent contrast can be color-coded to enhance the visualization of hidden biological structures that may be hard to see from typical OCT images. The results from Chapter 2 confirmed that the inherent contrast of OCT is reliable to detect the small structural defects. The following chapters demonstrate another type of OCT's inherent contrast that is based on elastography technique. Elastography can identify the small mechanical property changes in biological tissue.

Chapter 3: 1st approach to developing OCE

Section 3.1: Specification of OCT

The fiber-based spectral-domain OCT system used in this dissertation study was hand-built in our laboratory. This single mode fiber-based spectral-domain OCT system is capable of acquiring intensity information of biological tissue at a maximum camera acquisition rate of 45 kHz. The light source utilized during the experiment consisted of two super luminescent diodes (SLD) with a combined center wavelength of 1,298 nm and a 120nm full-width half-maximum bandwidth. The source of light was sent through a fiber optic circulator and a 20/80 splitter. The splitter divided the light between the sample arm and the reference arm, where 20 percent resulted in the reference arm and 80 percent resulted in the sample arm. At the sample arm, two-dimensional (2-D) raster scanning was achieved by the optical beam scanning across the biological sample using two galvanometer mounted mirrors and focused by a 30mm focal length lens. Subsequently, the light reflected off the mirror in the reference arm and the biological tissue in the sample arm recombined at the splitter and redirected through the circulator onto a grating. Upon reaching the grating, the light dispersed and became detected in the line scan camera. The depth profile was achieved in each spectrum acquired by the camera and provided specific depth information in each specific location pre-determined in the sample. The depth-resolved structural information was retrieved after linearly remapping to k-space from each A-line by applying a Fourier transformation to the spectrum collected on the camera. The images achieved were displayed on an inverse log scale. To achieve real-time visualization of the sample, a software was developed in our

laboratory by utilizing a graphic processing unit (GPU). The software allowed for acquiring, processing and displaying of the OCT cross-sectional image in real time [46]. The OCT system achieves an axial imaging range of approximately 2 mm within the biological tissue, defined an axial resolution of 8 μm and a lateral resolution of 20 μm.

Section 3.2: Fringe washout effect based OCE

As previously mentioned, the axial motion causing the fringe washout is introduced by implementing external ultrasound or shock wave perturbation. In theory, the ratio of the OCT intensity measured during the mechanical perturbation to that measured without mechanical perturbation can be directly correlated to the induced perturbation displacement of the tissue. This relative measure of depth-resolved tissue displacement (strain) is strongly correlated to the mechanical properties of a sample. In a region where the tissue is either dense or mechanically stiff, the scatterers displacement responds to a given acoustic power smaller than that in a region where the density or mechanical stiffness of the tissue is lower.

Analysis of the fringe washout can be achieved by comparing the detected intensity of the tissue at non-perturbed and perturbated conditions. The intensity detected at the CCD, that is interference signal between light reflected back from the reference and sample arms interfere can be expressed as:

$$I(k) = I_r(k) + I_S(k) + 2\sqrt{I_s(k)I_r(k)}\sum_n \alpha_n \cos(kz_n) \quad \text{(Eq. 1)}$$

where $I_r(k)$ and $I_s(k)$ are the wavelength-dependent intensities from the reference and the sample arms and α_n is the square root of the sample reflectivity at depth *n* under z_n. Optical power as a function of wavenumber read on a spectrometer at reflector from the sample arm at a given position z is $\alpha_n \cos(kz_n)$. The intensity at given acquisition time *T* can be expressed as:

(Eq. 2)

$$I_0(k, z_0) = \int_0^T \alpha \cos(kz_0)\, dt$$

where I_0 and z_0 are intensity and depth position respectively with the reflector at a constant position. This can further be expressed as:

(Eq. 3)

$$I_0(k, z_0) = T\alpha \cos(kz_0).$$

However, the position of the reflector at the sample arm is modulated by a perturbation pulse where the position of the reflector is no longer constant. The equation considering perturbation pulse and intensity at given camera acquisition time *T* can be expressed as:

(Eq. 4)

$$I(k, z) = \int_0^T \alpha\, cos\big(k(z_0 + z_n\, cos(\omega t))\big)\, dt$$

where ω is the frequency of perturbation pulse. Assuming a perturbation frequency is significantly greater than the integration time for a single depth profile where $\omega \ll 1$ and $kz_1 \ll 1$, the Eq. 2 can be modified by using Taylor series to give the intensity with mechanical perturbation as:

(Eq. 5)

$$I(k, z) = T\alpha \cos(kz_0)\left(1 - \frac{1}{4}k^2 z_n^2\right)$$

To a first approximation, the mechanical stiffness of a sample can be estimated through the ratio of intensity during the mechanical perturbation to that without as:

(Eq. 6)

$$\frac{I(k,z)}{I_0(k,z_0)} = 1 - \frac{1}{4}k^2 z_n^2$$

z_n is a perturbation induced displacement amplitude. OCT intensity information is typically displayed on a logarithmic scale, and given that the reflectivity is directly related to the measured OCT intensity, the ratio of intensity can be expressed as:

(Eq. 7)

$$\frac{I_{on}}{I_{off}} = 10^{\frac{(dB_{on} - dB_{off})}{10}} \quad \text{or} \quad \frac{I_{off}}{I_{on}} = 10^{\frac{(dB_{off} - dB_{on})}{10}}$$

where I_{off} is$I_0(k,z_0)$ and I_{off} is $I(k,z)$. Simple quantification of the ratio of intensity can be expressed as:

(Eq. 8)

$$\Delta dB = dB_{on} - dB_{off} = 10\log I_{on} - 10\log I_{off}$$
or
$$\Delta dB = dB_{off} - dB_{on} = 10\log I_{off} - 10\log I_{on}$$

where the intensity difference is simply the result of subtraction. Thus, the local mechanical tissue compliance can be estimated by taking the difference of the OCT intensities on a dB (logarithmic) scale [47].

To obtain the perturbation induced displacement amplitude z_n , we can derive the equation from Equation 6 that can be expressed as:

(Eq. 9)

$$z^2 = \frac{4}{k^2}\left(1 - \frac{I_{off}}{I_{on}}\right)$$

$$= \frac{4}{k^2}\left(1 - 10^{\frac{\Delta dB \Delta}{10}}\right)$$

Section 3.3: Speckle Noise

The previous speckle noise studies show that the variation in intensity attributed to fully developed coherent speckle is of the same order of magnitude of the OCT signal itself [48, 49]. This speckle noise introduces an artifact in OCT images and demonstrates that the standard deviation of coherent speckle in OCT images on the same order of magnitude as the mean intensity obscures identification of small regions and layers of biological tissue in OCT images. Since a significant portion of fringe washout based OCE analysis relies on localized comparison between images acquired with and without mechanical perturbation, it is possible that the presence of speckle makes localized characterization of cartilage difficult. It is also expected that the magnitude of tissue motion caused by the relatively low power of the external perturbation is insufficient to significantly alter the speckle pattern between consecutive depth profile acquisitions.

Thus, we expect that simple averaging with a kernel larger than the size of a speckle grain significantly reduces any remaining artifact. Figure 3.1 shows the OCT intensity images of a sample rat knee cartilage with different size of averaging kernel applied. The optimal amount of speckle noise reduction can clearly indicate the layers between calcified and collagen regions in the second image with the zoomed in area.

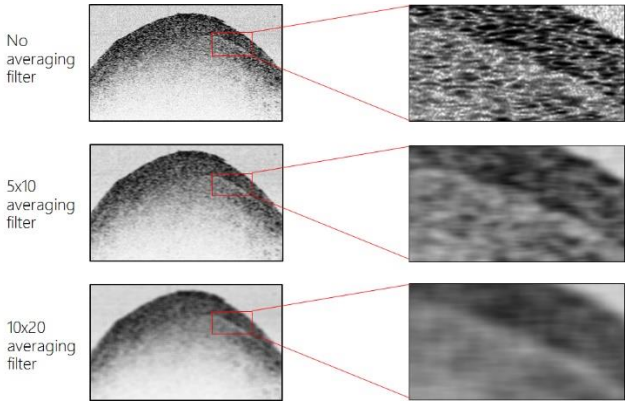

Figure 3.1 OCT intensity images with different averaging kernel size. No averaging filter was applied (top). 5x10 averaging filter was applied (middle). 10x20 averaging filter was applied (bottom). The optimal averaging filter was determined to be the middle image.

In a careful manner, characterization of the spatial resolution, mechanical assessment sensitivity and requisite OCT signal level for a reliable detection of an OCE signal are performed using agar and plastic phantoms in comparison to Young's modulus measurements using atomic force microscopy (AFM). The experimental methods were expected to demonstrate a clear correlation between the intensity difference derived from OCE images for various densities of agar and plastic phantoms with Young's modulus and spans to the *in vitro* study with arthritis induced rat knee cartilages. We further characterize and compare the spatial resolution for this mode of detection in mechanically heterogenous samples and the local mechanical properties measured by AFM.

Section 3.4: Proof of concept – experimental methods

This section describes the first approach to develop the OCE technique based fringe washout effect. The main purpose of the first approach was to establish the proof of concept of fringe washout based OCE technique. The first phase was to optimize the OCE apparatus including the experimental setup, angle of ultrasound perturbation to

sample, frequency of ultrasound to the OCE acquisition speed and post-processing technique. This characterization process was achieved with a tissue phantom study that represented mechanical property changes within samples. The results were correlated to atomic force microscopy (AFM). Finally, an *in vitro* study was carried with arthritis-induced animal models to demonstrate the capability of the OCE technique. AFM analysis was applied to the *in vitro* study to correlate the results once again.

Section 3.4.1: Function generator driven ultrasound OCE apparatus

The first approach was to use a function generator (Stanford Research Systems Model DS345) with an ultrasound transducer (Olympus V318-SM, 0.5 MHz, 0.75" diameter) as a source of mechanical perturbation. This combination was chosen to simplify the OCE apparatus in order to overcome intensive hardware and software modification. This ultrasound perturbation apparatus is capable of producing ultrasound pulses of <1.0V amplitude up to 500kHz frequency. Figure 3.1 shows the ultrasound perturbation power measured in a water chamber reaching samples in 50mm. The ultrasound perturbation power was received by an ultrasound receiver and displayed with an oscilloscope.

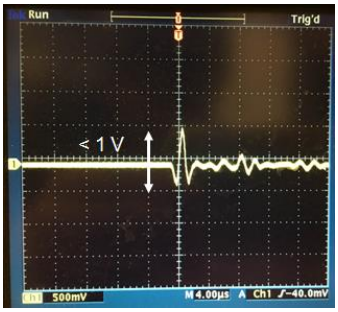

Figure 3.2 Function driven ultrasound perturbation power measured in an oscilloscope.

50mm was determined to be the optimal length since the perturbation power did not change over the short length of traveling in the water. Moreover, 50mm was optimal for the OCE apparatus configuration shown in Figure 3.3.

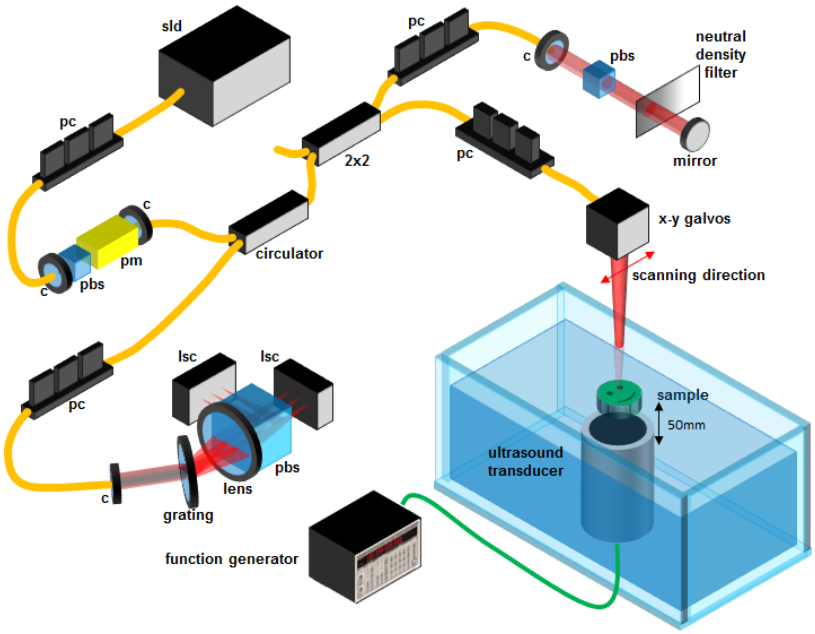

Figure 3.3 Schematic of the OCE system employing function generator driven ultrasound perturbation system. sld: superluminescent diode (broadband light source), pc: polarization controller, pbs: polarization beam splitter, pm: electro-optic polarization modulator, c: fiber collimator, lsc: line scan camera.

The OCT sample arm was placed above water in a chamber where imaging samples were placed. The water chamber was constructed and filled with water for ultrasound pulses to travel to the samples. The ultrasound transducer probe was placed under the sample shown in Figure 3.3. This ultrasound transducer placement was considered the ideal mechanical perturbation to introduce maximum fringe washout effect in scatterers of samples in an axial motion rather than a transverse motion [11]. The transducer angle α, which is the angle between the OCT sample arm to the ultrasound transducer, was set to

be 180 degrees as shown in Figure 3.3 above. For the proof of concept, the fringe washout based OCE, Figure 3.3 was setup to acquire OCE information of biological samples.

Section 3.4.2: Characterization of OCE with tissue phantom study

As described in the fringe washout theory, the relative measurement of strain is strongly correlated to the depth-revolved sample scatterers displacement. In a region where the sample is either dense or mechanically stiff, the displacement of scatterers responds to a given ultrasound perturbation would be smaller than that in a region where the density or mechanical stiffness of the sample is lower. This rapid axial motion induced displacement of scatterers in the sample caused the fringe washout in acquired OCT intensity information. This fringe washout caused the decrease in intensity signal comparing to the scatterers without axial motion. This displacement of scatteres (strain) can be quantified by calculating the amount of decreased intensity signal and comparing it to the steady state by taking the difference intensity. The intensity difference in dB scale was calculated by a simple subtraction of the intensity signal with and without an ultrasound perturbation acquired by OCT system.

The intensity difference was calculated by post-processing after the data was acquired. MATLAB numerical computing environment was used for the post-processing, we developed our own processing codes for the interpretation of the OCE data. The concept of the OCE post-processing is based on matching two similar images and subtracting one from another. Our OCT system can image the same area over the course

of time using two-dimensional (2-D) raster scanning at the OCT sample arm and by configuration of two galvanometer mounted mirrors. This allows the OCT system to scan the exact same area multiple times by fixing the positon of the sample. Since the OCT system was capable of imaging the same area over the course of time, the OCT intensity data with and without ultrasound perturbation were acquired. In subtracting one image frame of OCT intensity data from one image to another without ultrasound perturbation, we can extract the decreased intensity signal by using axial scatterers displacement causing fringe washout. Figure 3.4 shows the idea of this post-processing. As described above, this decreased intensity or the intensity difference signal is strongly correlated to the mechanical properties of a sample. Thus, the lower intensity difference calculated in dB scale indicate how stiff the mechanical property is.

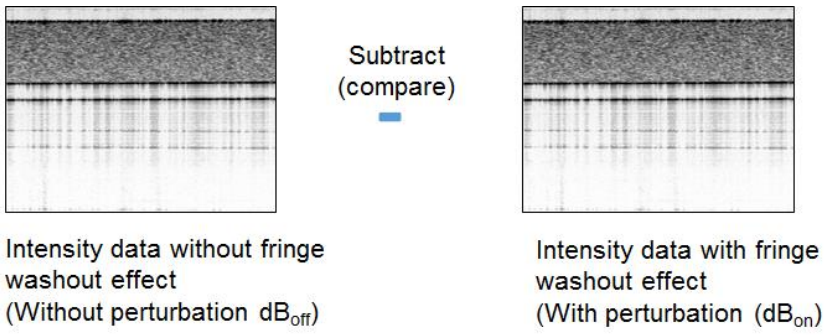

Figure 3.4 Basic OCE post-processing and analysis

In the initial proof-of-principle of the OCE technique, the tissue phantom study was carried to test its capability. The tissue phantom model is prepared with common ballistic gelatin to mimic the human model. By using the various densities of agar (Fisher Scientific BP1423-500) samples, the characteristic of tissue stiffness that occurs during OA progression is replicated. The stiffer biological tissue is replicated by increasing agar

density, whereby higher agar density samples are stiffer in isotropic materials. The agar densities were prepared in the way that 10g of the agar resolved in 100mL of distilled water were indicated as 10% density. An intralipid 2% homogeneous solution was also added to the samples for scatterers. The agar samples were prepared in 2%, 3%, 4%, and 5% density.

Before proceeding to the tissue phantom study, setting optimal ultrasound pulse parameters and OCT acquisition parameters were necessary to maximize the fringe washout effect. In the 2% density agar sample used, two images with and without ultrasound perturbation were acquired for each parameter setting, and the intensity difference was calculated for each sample during post-processing. The imaging area was set to 6mm x 2mm in cross-sectional area composed of 2048 a-lines. There were some limitations to the ultrasound pulser hardware. Since the function generator can provide the amplitude from 0V to 10V, the maximum amplitude was limited to 10V. The frequency of ultrasound pulses needed to be few times faster than the OCT acquisition speed in order to capture the displacement of the scatterers induced by ultrasound perturbation. In order to achieve intensity difference, the ultrasound frequency was set to the low end at 100kHz, and the high end was set to 500kHz. Figure 3.5 shows the result of calculated intensity difference values for each parameter setting.

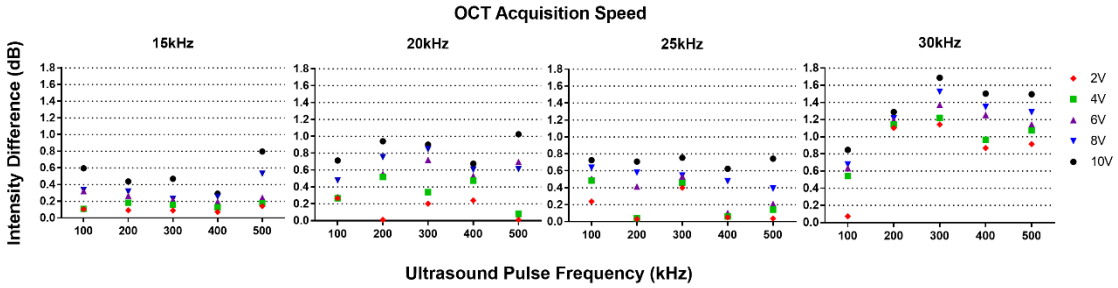

Figure 3.5 Different combination of OCT acquisition speed, ultrasound pulse frequency (kHz) and ultrasound amplitude parameter settings for OCE. Intensity difference was quantified for each setting.

The result of this test showed that the ultrasound and OCT acquisition parameters should be set to 300kHz frequency and 10V amplitude for ultrasound pules, and OCT acquisition speed to be 30kHz. This setting combination provides the most intensity difference which was correlated to the magnitude of induced fringe washout.

A tissue phantom study was conducted with optimal parameter settings as described above. The prepared agar samples in 2%, 3%, 4% and 5% density were used. Each sample was imaged with and without ultrasound perturbation and post-processed to calculate the intensity difference in the dB scale. Figure 3.6 shows the result of the calculated intensity difference for each different agar density. Figure 3.6 shows the clear trend in the dense agar sample, the stiffer the material, the lower the intensity difference value. This proves that the OCE technique provides the assessment, but further verification was needed on the trend of the mechanical property of each agar sample.

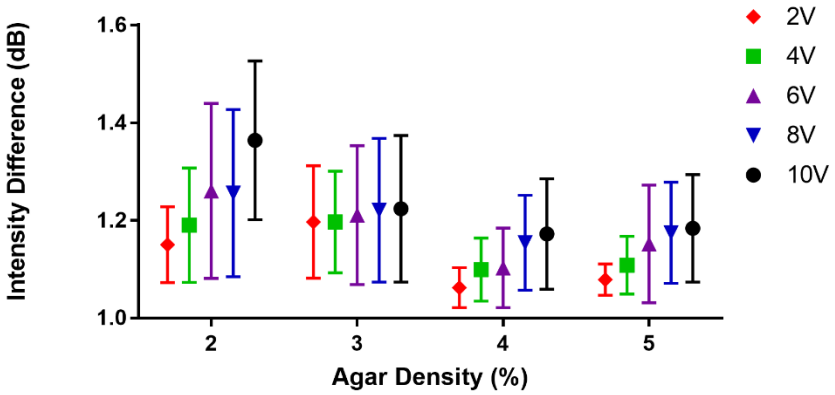

Figure 3.6 Calculated intensity difference in dB at difference amplitude of ultrasound pulse for difference agar density (%)

Section 3.4.3: Tissue phantom study with atomic force microscopy (AFM)

To verify the OCE intensity difference data of the same agar samples, measurement of the Young's modulus values with atomic force microscopy (AFM) was conducted. Young's modulus is one of the most common measurements that indicates stiffness of materials. AFM is a common method used to measure and quantify the property of elastic isotropic material. The AFM measurement was carried to quantify the stiffness of the samples at the same region where the OCE intensity difference assessment was conducted. This correlation experiment justifies the trend in OCE intensity difference where the stiffer mechanical property has lower intensity difference.

A MFP-3D AFM (Asylum Research, Santa Barbara, CA.) was used to measure the Young's Modulus values of the samples. AFM was in a forced mode using a 0.6 N/m silicon nitride tips modified with an attached 20 µm borosilicate sphere (Novascan Tachnologies, Ames, IA.) for the tissue phantom study. A 5.4 N/m silicon cantilever tips modified with an attached 5 µm borosilicate sphere was used for the in vitro study with knee cartilage samples. AFM was set at an indentation and retraction speed of 2 µm/s

and a set trigger force of 50 nN in order to survey a macroscopic region of each samples. The measurement was carefully executed within fluid to avoid tip-sample adhesion and dehydration. Values for the Young's Modulus of each sample were calculated by fitting the force indentation curve with the Hertz theory model for spherical indenters [50],

$$F = \frac{4E\sqrt{R}}{3(1-\upsilon^2)}\delta^{3}/_{2}, \quad \text{(Eq. 7)}$$

where F is the force measured by the indenting tip, E is the Young's modulus of the material being tested, R is the radius of the glass sphere, υ is the materials Poisson's ratio, and δ is the indentation depth of the glass sphere. For the agar samples, a Poisson's ratio of 0.33 [51] was used for fitting the data. The AFM measurements were carried to each sample immediately after the OCE imaging to avoid its degradation.

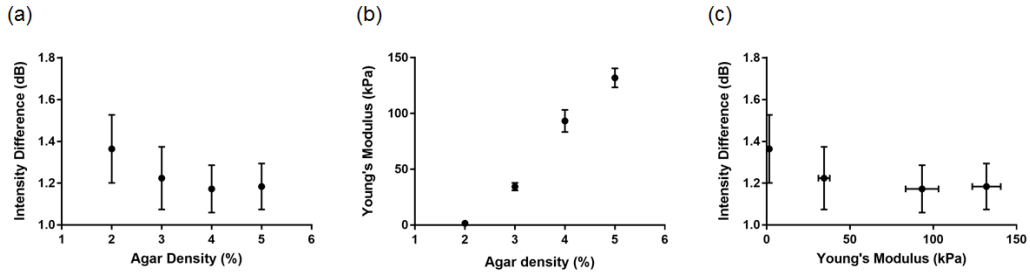

Figure 3.7 (a) Calculated intensity difference (dB) for each agar density. (b) Measured Young's modulus value for each agar density. (c) intensity difference for each agar density compared to measured Young's modulus for each agar density.

Figure 3.7 (a) shows the intensity difference calculated by the OCE system for the agar samples. Figure 3.7 (b) shows Young's modulus measurements by the AFM system of the same samples. The same region of agar samples used to calculate the intensity

difference and Young's modulus values were the same. FIGURE (a) and (b) illustrate the strong correlation between the intensity difference values to the Young's modulus values that the mechanical property of samples became stiffer. The OCE intensity difference can provide relative quantification of stiffness in mechanical property.

Section 3.5: *In vitro* study with arthritis induced rat cartilage

The tissue phantom study provided a strong proof of the fringe washout based OCE technique. However, the mechanical property changes replicated with different agar density samples during the phantom study was physical change that the stiffness was considered to be homogenous through each sample. The micro-scale property change was hard to replicate with the agar sample study. In this section, the OCE study was conducted with *in vitro* animal models to perform the OCE technique. The osteoarthritis induced rats were used for the *in vitro* animal model, and were prepared with monosodium iodoacetate (MIA) injection.

Section 3.5.1: Osteoarthritis induced rats model (MIA model) preparation

Osteoarthritis induced rats knee cartilages used in *in vitro* study were prepared with monosodium iodoacetate (MIA) injection to create the osteoarthritis condition in rat knee samples. All preparation, procedures and animal handling for the *in vitro* studies approved by Institutional Animal Care and Use Committee (IACUC) at University of California, Riverside were used. Twelve skeletally mature female Sprague-Dawley rats between 12-14 weeks old were anesthetized with isoflurane and then a single intra-

articular injection of monosodium iodoacetate (MIA) in the right knees was administered to induce cartilage damages (2mg in 50 mL saline per knee). The animals were randomly divided into 4 groups, and Group 1 were sacrificed on day 0 (MIA-day 0, control), Group 2 on day 3 (MIA-day 3), Group 3 on day 5 (MIA-day 5) and Group on day 11 (MIA-day 11). From the previous studies [52, 53], it was determined that the cartilage damages on day 0, day 3, day 5 and 11 correspond to grade 0, 0.5, 1.0 and 1.5 respectively in the Pritzker's grading system [54]. Tibias were excised and the specimens were fixed and stored in 10% formalin until further processing. These samples were imaged with the OCE technique and the results are discussed in following sections.

Section 3.5.2: *In vitro* study with OCE

The cartilages from medial side of MIA-day 0 (control) tibia, MIA-day 3, MIA-day 5 and MIA-day 11 were imaged with our OCE technique employing ultrasound perturbation in the direction shown in Figure 3.8. The parameters for the OCE system were set to be 300kHz frequency and 10V amplitude for ultrasound pulser and OCE acquisition speed to be 30kHz. The distance between the ultrasound transducer probe and sample is set to be 50mm. All the parameters were chosen to optimize the OCE acquisition. Two different OCT intensity images of a knee sample with and without ultrasound perturbation were acquired in cross-sectional size of 6mm x 2mm.

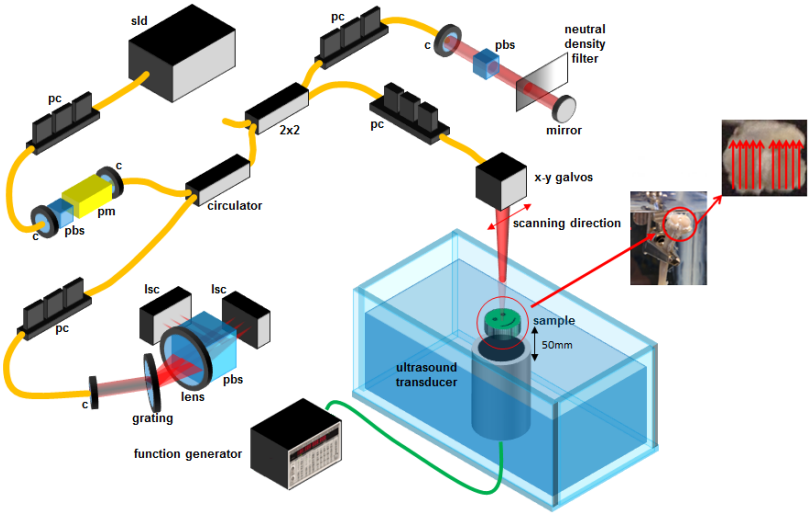

Figure 3.8 Schematic of the OCE system with a MIA model knee sample in place. The OCE imaging direction (scanning direction) and ultrasound perturbation direction are shown.

The same OCE post-processing analysis described above was employed. The basic idea of this post-processing was to extract the OCT intensity decreased signal by axial scatterers displacement causing fringe washout. We subtracted one OCT intensity image with ultrasound perturbation from one OCT intensity image without ultrasound perturbation. The remaining intensity signal, which is the intensity difference, indicated the relative assessment of mechanical property stiffness of the knee samples. Figure 3.9 shows the post-processed OCT intensity image to indicate the area that was used to calculate the intensity difference.

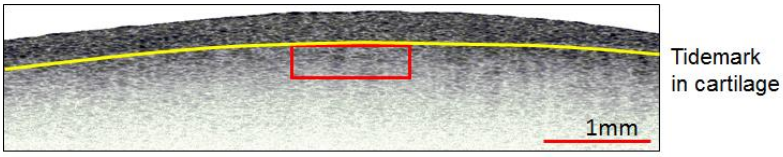

Figure 3.9 The red box indicates the region in cartilage where the intensity difference was calculated. The area is just below the tide mark.

The red box indicated the region where the intensity difference was calculated and averaged for each sample. Each knee sample was conducted with 10 different OCT intensity cross-sectional imaging sets on the same region of interest. The averaged intensity difference over the red-box region was calculated for each time. The results were shown in Figure 3.10. The control knee sample had the relatively higher intensity difference in values comparing to the other arthritis progressed knee samples of MIA-day 3, MIA-day 5 and MIA-day 11.

In theory, stiffness of knee gets higher as osteoarthritis progresses. The intensity difference trends from the result indicated that the stiffer the knee sample, as osteoarthritis progressed, had lower the intensity difference values. This result follows the assumption that the displacement of scatterers in a stiff sample is smaller giving a lower fringe washout resulting in a lower intensity difference value. Thus, our OCE technique can provide the relative assessment of mechanical property of stiffness in *in vitro* samples.

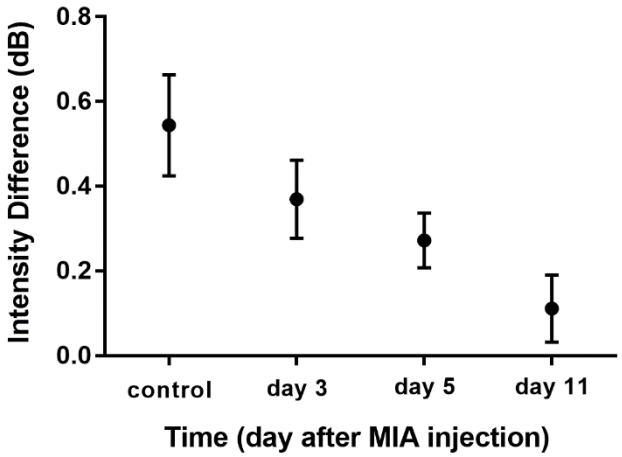

Figure 3.10 Calculated intensity difference (dB) for each MIA model.

Section 3.6: Conclusion

In Chapter 3, we demonstrated the possible alternative technique for OCE and the first approach to develop our fringe washout based OCE system. The purpose of this chapter was to demonstrate the concept of fringe washout based OCE method to detect mechanical property change of strain in samples. The tissue phantom study was successfully carried and OCE technique was able to distinguish the different stiffness of agar samples with calculating the intensity difference value. Young's modulus values measured by AFM technique verified that each agar sample had different stiffness. This was the first step to confirm the ability of our OCE technique.

We demonstrate the feasibility of our OCE technique in *in vitro* study with arthritis-induced rats model (MIA model). This study was performed to evaluate our OCE technique with heterogeneous samples instead of homogeneous samples as agar samples. As the tissue phantom study, the intensity difference values were calculated for MIA-day 1, MIA-day 3, MIA-day 5 and MIA-day 11. Distribution of the calculated intensity difference values were shown as standard deviation bars in Figure 2.9. This concludes the feasibility of our OCE technique in real samples.

However, there are few limitations and disadvantages of the first approach that need to be overcome for the better OCE system. First, the ultrasound perturbation power was not enough to significantly differentiate between samples with small intensity difference values. The difference in the intensity difference value of control and MIA-day11 achieving less than 1 dB was not substantial. To successfully identify the small mechanical property changes between samples, the intensity difference between two

consecutive samples need to be more than 1 dB. Second, the imaging requires two sets of data, one with and one without ultrasound perturbation. This requirement results in mismatching the exact region of interest in samples that this OCE technique can lead to inaccurate OCE results. To prevent this inaccuracy, an alternative idea is to extract both intensity information with and without mechanical perturbation from one set of data. Third, the imaging is still limited to cross-sectional images where volumetric imaging is not feasible. This incapability comes from insufficient way to acquire OCE images. To overcome this limitation, synchronizing the mechanical perturbation to the OCT acquisition needs to be implemented. This synchronization can be a solution to the second limitation in the list and it can maximize the fringe washout effect.

Chapter 4: 2nd approach to developing OCE

Section 4.1: Introduction to shock wave

The previous approach did prove the concept of fringe washout based OCE technique. However, there were disadvantages where the OCE system failed to provide accurate mechanical property information of the samples. The purpose of this chapter is to overcome one of the disadvantages. The major disadvantage was weak perturbation power of ultrasound from the previous approach. The optimal mechanical perturbation causing axial displacement in scatterers of samples is the key to introduce the right amount of fringe washout. The right amount of fringe washout is that the modulation of scatterers in response to external perturbation is smaller than the image pixel size.

In this chapter, we used shock wave as a new perturbation source. The procedure for developing another approach to the fringe washout based OCE was similar to the first approach. First part was to optimize the OCE apparatus including the experimental setup, angle of ultrasound perturbation to sample, frequency of ultrasound to the OCE acquisition speed and post-processing technique. This characterization process was achieved with a tissue phantom study that replicated mechanical property changes within agar samples. The results were correlated to atomic force microscopy (AFM). Finally, *in vitro* study was conducted with osteoarthritis induced animal models to demonstrate the capability of the OCE technique. AFM analysis was applied to the *in vitro* study to correlate the results once again.

Section 4.1.1: Shock wave OCE apparatus

The second approach for our OCE technique used shock wave as a mechanical perturbation source. Our OCE introduced the use of a VersaTron 4 Paws (Model: 4Paws with its energy flux 0.15 mJ/mm^2) manufactured by PulseVeterinary Technologies into the OCE system. The VersaTron 4 Paws generated a high-energy acoustic pressure wave (shock wave) to the OCE sample arm. The trode of the VersaTron was placed in an angle (α) relative to the OCT scanning direction as shown in Figure 4.1. The α was pre-determined to maximize the shock wave penetration in the water-filled chamber designed to accommodate a biological tissue with shock wave trode as well as considering the stability of the trode. Dr. Yun Hu's publication proved that the axial motion of scatterers in tissue caused more fringe washout effect in OCT depth profile acquisition than the transverse motion did [11]. We placed the trode in an angle of 45 degrees to introduce axial motion to samples. This angle was also considered to protect the OCE sample arm from the shock wave perturbation that shock wave pulses did not distract the sample arm imaging. The distance between the trode to the samples were set to be 50mm for the safety of the OCT sample arm as well as preserving the perturbation power.

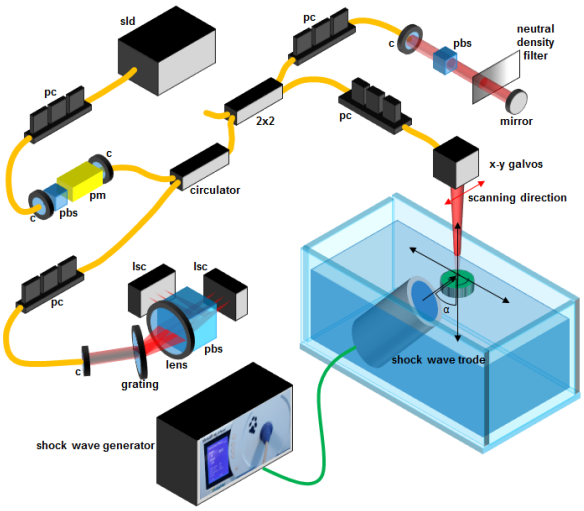

Figure 4.1 Schematic for the OCE system employing shock wave perturbation.

Each image was composed of 2048 A-lines acquired at a 30kHz camera speed over the period of time at the same location. During the time period, we acquired OCT intensity information with and without the shock wave perturbation. The shock wave pulse was set to a maximum rate of 6 pulses/sec to capture as much shock wave pulses as possible during the OCT image acquisition procedure.

Section 4.1.2: Characterization of OCE with tissue phantom study

Since the shock wave propagated differently compared to ultrasound, the post-processing to calculations of the intensity difference was not a simple subtraction as described in Chapter 3. However, the basic concept of calculating the intensity difference in the dB scale was a direct result of subtracting of the OCT intensity data acquired with and without shock wave perturbation. This required this OCE technique to acquire two different set of intensity data at the same imaging region. This intensity difference was the result of decreased intensity signal caused by fringe washout that shock wave induced

axial displacement to the scatteres in the sample during the OCT acquisition as described above. Thus, the intensity difference can provide relative measurements of strain in samples where the mechanical stiffness of the sample is lower, the intensity difference is higher.

MATLAB numerical computing environment was used for the post-processing and analysis that we specifically developed our own processing codes for the OCE shock wave data. Due to high perturbation power of shock wave, the shock wave induced fringe washout effect can be observed easily on images. Figure 4.2 shows a captured shock wave pulse in an OCT intensity image of an agar sample. Since the shock wave perturbation was set to 6 pulses/sec and OCE image acquisition rate was set to 30kHz acquisition speed with 2048 a-lines over 6mm x 2mm imaging range, the delivery of shock wave pulse was captured in each OCT image. The fringe washout area in an OCT image was used to calculate the OCT intensity during shock wave perturbation.

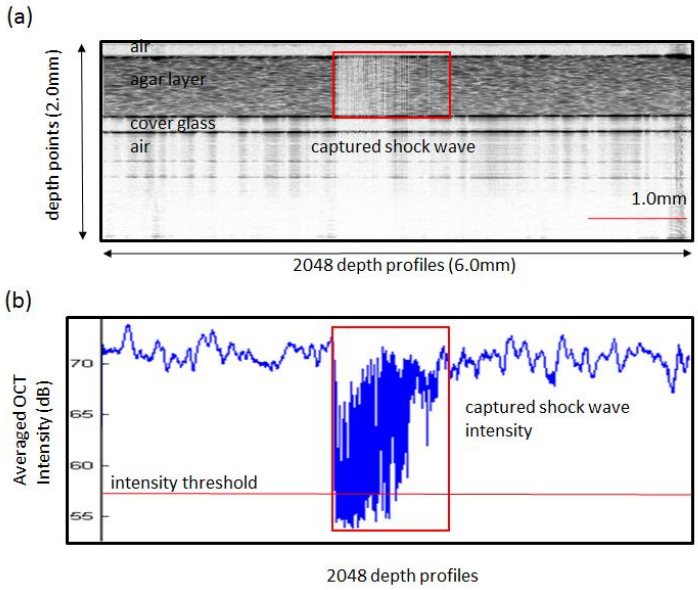

Figure 4.2 (a) an OCT intensity image capturing a shock wave pulse with in a cross-sectional frame. (b) a plot of the average intensity value of the agar layer over 2048 depth profile points.

The first step of the analysis was to extract the fringe washout data from shock wave captured data. Since a shock wave pulse was captured in a portion of an intensity image, extracting the area of the image containing the fringe washout effect was needed to calculated the intensity difference. To extract the shock wave captured area in the image, the threshold on intensity data was set to filter out other area. Figure 4.2 shows the extraction of shock wave captured area by setting the threshold in intensity values. This shock wave captured area in an OCT image was used for the intensity data with shock wave perturbation.

Second step was to modify the OCE acquisition technique. Since the acquisition was set to capture one shock wave pulse at random a-lines locations in one OCT image frame, construction of a whole cross-sectional OCT image with shock wave perturbation throughout the image needed to be achieved by reconstructing the image with many

shock wave pule captured images. To accomplish this technique, the feature of our OCT system provided an advantage. Our OCT system can image the same area over time by the two-dimensional (2-D) raster scanning capability at the OCT sample arm with the configuration of two galvanometer mounted mirrors. This allowed the OCT system to scan the exact same area of the samples if the sample did not move its position. The reconstruction of the cross-sectional OCT image with shock wave perturbation needed to take roughly about 1000 shock wave pulse captured OCT cross-sectional images. By setting the threshold at the intensity signal described in first step above, we could extract a shock wave pulse perturbated intensity from a specific a-lines location and placed it to the corresponding a-lines location in the empty image matrix array. The empty image array was filled with shock wave perturbated intensity by repeating this extraction process over 1000 times. Figure 4.3 shows the reconstruction process of filling the empty image array.

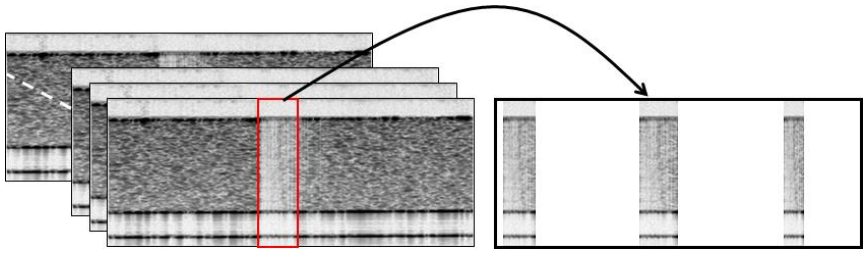

Figure 4.3 The construction of fringe washout induced OCT intensity image in empty array.

Subtracting the reconstructed image of shock wave perturbated data from the OCT intensity image data without perturbation was achieved in order to calculate the intensity difference and construct the OCE image. Figure 4.4 (a) shows the OCT intensity cross-sectional image without the shock wave perturbation. The same agar samples at the same

region of interest were then imaged with the shock wave perturbation. Since the shock wave perturbation was captured at random a-line locations in each image shown in Figure 4.4 (b), scanning the same area over time to acquire 1000 image frames of shock wave perturbation captured were used to construct one shock wave perturbated image shown in Figure 4.4 (c). The intensity difference in the dB scale were simply calculated by subtracting the intensity values acquired at the shock wave perturbation from the intensity values acquired without the shock wave perturbation ($dB_{off} - dB_{on}$). Consequently, Figure 4.4 (c) was subtracted from Figure 4.4 (a) to create Figure 4.4 (d). Figure 4.4 (d) shows the heat map representing the intensity difference values. The heat map was generated in the way that higher intensity difference area is shown in red-colored and lower intensity difference area as blue-colored.

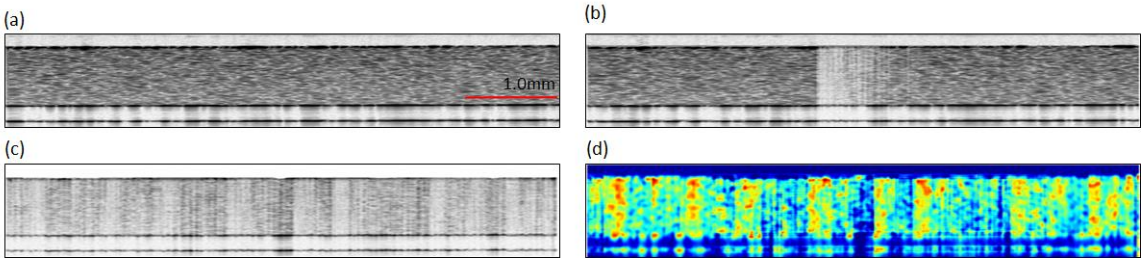

Figure 4.4 (a) An OCT intensity image frame without shock wave perturbation. (b) An OCT intensity image frame capturing a shock wave pulse. (c) A fringe washout induced OCT intensity image frame. (d) An OCE image frame of calculated intensity difference.

The subtraction was able to extract the intensity decreased signal by axial scatterers displacement causing fringe washout. As described above, this decreased intensity or the intensity difference signal is strongly correlated to the mechanical properties of a sample. Thus, the lower intensity difference calculated in the dB scale indicate stiffer the mechanical property.

In the initial proof-of-principle of the OCE technique, the tissue phantom study was conducted to test its capability. The tissue phantom model was prepared with ballistic gelatin to mimic the human model. By using the various densities of agar (Fisher Scientific BP1423-500) samples, the characteristic of tissue stiffness that occurs during OA progression is replicated. A stiffer biological tissue was replicated by increasing agar density for stiffer isotropic materials. The agar densities were prepared in the way that 10g of the agar resolved in 100mL of distilled water would be indicated as 10% density. An intralipid 2% homogeneous solution was also added to the samples for scatterers. The agar samples were prepared in 2%, 4%, 6%, 8% and 10% density. The same intensity difference analysis was applied to various agar density samples prepared previously. Figure 4.5 shows the result of the calculated intensity difference for each different agar density. Figure 4.5 shows the clear trend that the dense agar sample, which is stiffer the material, has lower intensity difference value. This is to prove that the OCE technique provides the assessment, yet the mechanical property of each agar sample needed for verification on the trend.

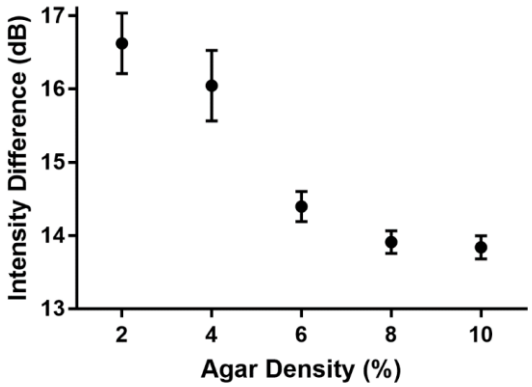

Figure 4.5 Calculated intensity difference in dB scale for each agar density sample.

Section 4.1.3: Tissue phantom study with AFM

The AFM strain analysis was performed to verify the mechanical properties of the same agar samples at the area with the Young's modulus values as well as correlating the intensity difference analysis of the OCE technique. As described in Chapter 3, AFM is one of common techniques to measure property of elastic isotropic material. In this case, Young's modulus was calculated to indicate stiffness of materials. To recall the AFM analysis, A MFP-3D AFM was in a forced mode using a 0.6 N/m silicon nitride tips modified with an attached 20 μm borosilicate sphere for the tissue phantom study with intralipid agar samples. It was set at an indentation and retraction speed of 2 μm/s and a set trigger force of 50 nN in order to survey a macroscopic region of each samples. The measurement was carefully executed within fluid to avoid tip-sample adhesion and dehydration. Values for the Young's Modulus of each sample were calculated by fitting the force indentation curve with the Hertz theory model for spherical indenters [50],

$$F = \frac{4E\sqrt{R}}{3(1-\upsilon^2)}\delta^{3/2}, \quad \text{(Eq. 7)}$$

where F is the force measured by the indenting tip, E is the Young's modulus of the material being tested, R is the radius of the glass sphere, υ is the materials Poisson's ratio, and δ is the indentation depth of the glass sphere. For the agar samples, a Poisson's ratio of 0.33 [51] was used for fitting the data. The AFM measurements were carried to each sample immediately after the OCE imaging to avoid its degradation.

AFM measurement was carried for the same samples at the same region where the OCE technique measured the intensity difference. Figure 4.6 (a) shows the intensity difference calculated by the OCE system for the agar samples. Figure 4.6 (b) shows Young's Modulus measurements by the AFM system of the same samples. Figure 4.6 (c) shows the combined plot of the intensity difference data from Figure 4.6 (a) and the Young's Modulus data from Figure 4.6 (b).

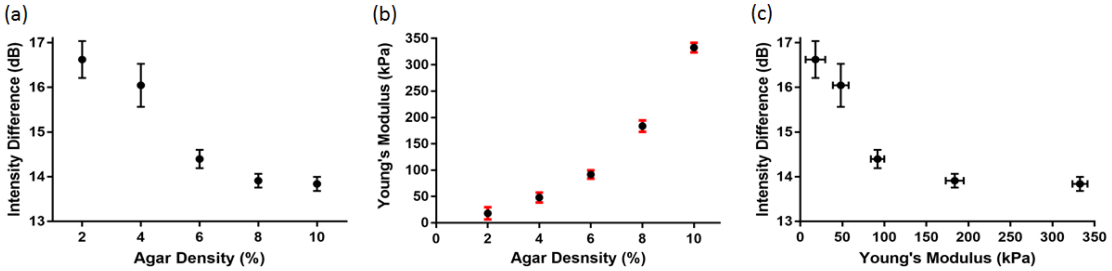

Figure 4.6 (a) Calculated intensity difference for each agar density sample. (b) Measured Young's modulus values over difference agar density samples. (c) Calculated intensity difference for each agar density compared to measured Young's modulus for each agar density.

Figure 4.6 illustrates the strong correlation between the intensity difference in dB scale to the Young's modulus values from the agar samples. The correlation between the mechanical property and the intensity difference can be stated that the stiffer agar samples have lower the intensity difference. This verification experiment justifies the OCE technique can assess the stiffness of the mechanical property with intensity difference.

Section 4.2: *In vitro* study with arthritis induced rat cartilage

For the osteoarthritis-induced rats model study, the remaining samples prepared from the Chapter 3 were used. To recall the preparation of the animal model, arthritis condition was induced to the right knees of nine, 12-14-week-old skeletally mature female Sprague-Dawley by a single intra-articular injection of MIA (2mg in 50 mL saline per knee). The animals were randomly divided into 4 groups, and each group was sacrificed on 0 day (control), 3rd day (MIA-day 3), 5th day (MIA-day 5) and 11th day (MIA-day 11). MIA-day 0, MIA-day 3, MIA-day 5 and MIA-day 11 corresponded to the cartilage damages based on Pritzker's grading system as 0, 0.5, 1.0 and 1.5 respectively [52-54]. Tibias were excised and fixed in 10 % formalin.

Section 4.2.1: *In vitro* study with OCE

The knee cartilages from medial side of MIA-day 0 (control) tibia, MIA-day 3, MIA-day 5 and MIA-day 11 were imaged with our OCE technique set to 30 kHz acquisition speed with 2048 a-lines over 6mm x 2mm imaging range at 6 pulses/sec shock wave trode perturbation. Figure 4.7 shows the shock wave apparatus where the trode was placed at 45 degrees and 50mm away to the sample in the water chamber.

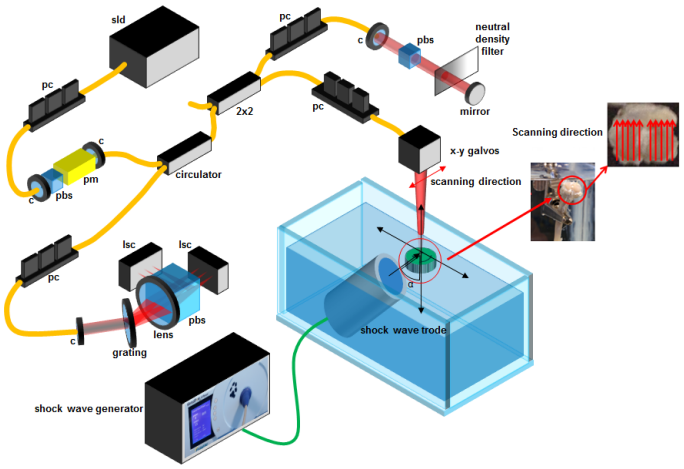

Figure 4.7 Schematic of the OCE system with a MIA model knee sample in place. The OCE imaging direction (scanning direction) and ultrasound perturbation direction are shown.

The same OCE analysis used in the tissue phantom study was applied to calculate the intensity difference and generate the heat maps. Figure 4.8 (a), (b), (c) and (d) are the OCT intensity cross-sectional images size 4 mm x 1 mm. Figure 4.8 (e), (f), (g) and (h) are the reconstructed intensity difference heat maps that were generated in the same manner as described in the tissue phantom study that used 1000 of pulse captured images. The heat maps are color-coded showing lower intensity difference values in blue and higher difference values in red.

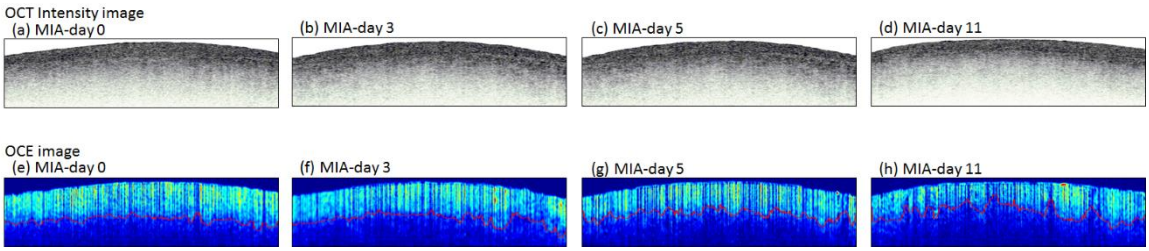

Figure 4.8 (a) (b) (c) (d) the OCT intensity images of MIA-day 0, MIA-day 3, MIA-day 5 and MIA-day 11. (e) (f) (g) (h) corresponding OCE images.

Each red-line in the heat maps Figure 4.8 (e), (f), (g) and (h) indicate the boundary between lower intensity difference and higher intensity difference based on the calculated intensity difference threshold. Comparing the depth locations of red-line boundary in Figure 4.8 (e), (f), (g) and (h), the red-line boundary in Figure 4.8 (h) is relatively higher in depth positions compared to Figure 4.8 (e), (f), and (g). Comparing the area below the red-line in Figure 4.8 (e), (f), (g) and (h), the blue-colored area occupies more in FIGURE (h). This could be a result from the characteristic of OA progression when calcification of the knee cartilage progresses from bottom of the medial meniscus to upper region. Thus, the red-line boundary defines the area between calcified and collagen in the cartilage.

Section 4.2.2: *In vitro* study with AFM

To verify this result from the OCE technique, the similar AFM technique described in the tissue phantom study above was applied to investigate the mechanical properties of the same samples. A MFP-3D AFM was used in a forced mode using a 5.4 n/m silicon cantilever tips modified with an attached 5 μm borosilicate sphere and set at an indentation and retraction speed of 2 μm/s and a set trigger force of 50 nN. The same cartilages were dissected to the same direction to the OCT imaging plane in the longitudinal direction. The Young's Modulus values were calculated at depth locations in the cartilage area for MIA-day 0 and MIA-day 11 samples. The depth locations were 50, 100, 150 200 and 250 μm below the cartilage surface. AFM acquired force measurement data over the course of depth in the longitudinal direction and calculated the corresponding Young's modulus values. The Young's Modulus values were the averaged

values of the area of 30 μm x 30 μm. The matching region of the cartilages were analyzed to calculate the intensity difference values. Corresponding data of the Young's modulus and the intensity difference values as a function of depth are shown in Figure 4.9.

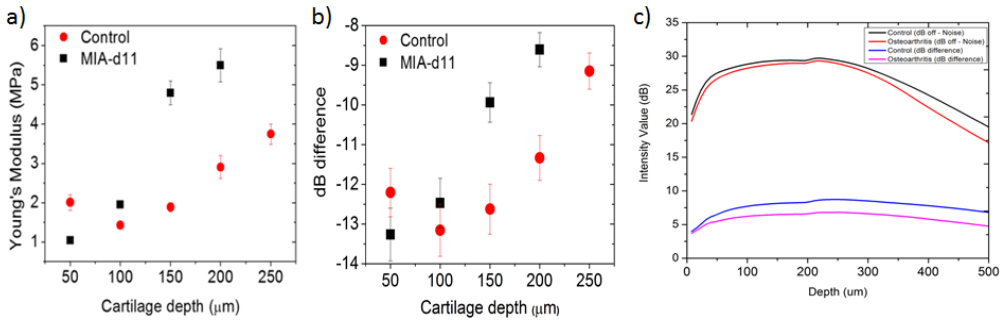

Figure 4.9 (a) Depth-dependent changes of intensity difference analyzed from OCE imaging, and (b) Young's modulus measured by AFM of control vs. MIA-day 11 damaged cartilage, showing similar trends that indicative of cartilage stiffening due to MIA. (c) OCE depth imaging limitation.

As confirmed in the tissue phantom study, the stiffer mechanical property region has the lower intensity difference value which the same tendency can be observed from Figure 4.9 (a) and (b). This result can show that the OCE technique is capable of applying in *in vitro* study to detect mechanical property changes in a specific region and that the relatively quantification with the intensity difference of the sample strain can be achieved.

However, the OCE technique has depth limitations caused by losing the backscattered light signal over the depth of the samples. Determining the depth limitation in length is crucial to understanding the difference between signal to noise from the samples. In comparing the pattern intensity difference values from MIA-day 0 and MIA-

day 11 in Figure 4.9 (c) confirms that the patterns are not caused by an artifact of noise existing in the imaging process nor the speckle effect from the scatterers. Thus, the OCE technique is considerably capable of assessing >250 μm in depth in cartilage samples.

Section 4.3 Conclusion

In the Chapter 4, we sought a solution to a weak perturbation power which was one of the disadvantages from Chapter 3. WE were able to use a shock wave generator was for our trial. One restriction we encountered was that the amount of shock wave pulses available for use was limited by the rental use agreement. Thus, the thorough characterization of shock wave and OCE with shock wave couldn't be performed for our project. Nonetheless, the alternative solution to one of the limitations mentioned in Chapter 4 was upon trial.

Shock wave is typically used for orthopedic therapy in order to stimulate anagiogenesis and neurogenesis to promote removing damaged matrix constituents and stimulating wound healing mechanisms [55]. Our assumption was to introduce a high magnitude of fringe washout during the OCT intensity acquisition by using powerful shock wave perturbation. The shock wave OCE system showed a significantly higher magnitude of fringe washout effect during the tissue phantom study with agar samples. The shock wave induced intensity difference was between 13 dB and 17 dB signal compared to the ultrasound induced intensity difference to be under 1 dB used in Chapter 3. The results from tissue phantom study demonstrated the capability of shock wave OCE technique to detect mechanical property change in stiffness of the agar samples. The OCE

intensity difference results were verified with corresponding Young's Modulus values measured by AFM where the agar samples with lower intensity difference had high stiffness features.

We also demonstrated the feasibility of our shock wave OCE technique in *in vitro* study with MIA model. As the tissue phantom study, the intensity difference values were calculated for MIA-day 0, MIA-day 3, MIA-day 5 and MIA-day 11 and Young's Modulus values were measured with AFM technique for each sample. The corresponding Young's modulus values verified that the stiffer mechanical property occurred in the later stage of arthritis-induced knee cartilage and had lower intensity difference values. Also, the shock wave OCE technique was able to identified the region of calcified knee cartilages as osteoarthritis had progressed. This concludes the feasibility of our OCE technique in real samples.

Although the shock wave OCE technique worked quite well on both tissue phantom study and *in vitro* study, there are few limitations and disadvantages of this second approach. First, the shock wave perturbation power was too powerful to induce fringe washout effect in OCT intensity images. Excessive perturbation power would introduce artifact in the images that remaining signals would reach to the noise floor. Although Figure 4.11 confirms that the intensity difference patterns were not caused by artifact of noise or the speckle effect from the scatterers in the samples, the ideal amount of fringe washout is based on decreasing signal at saturation of signal level itself [11]. Thus, the ideal amount of intensity difference is somewhere below 10 dB.

Second, the imaging still requires two sets of data that are with and without perturbation. In the shock wave case, acquiring over 1000 imaging frames was needed to reconstruct a shock wave perturbated image. This requirement results in mismatching the exact region of interest in samples that led to inaccurate OCE results. To prevent this inaccuracy, extracting both intensity information with and without mechanical perturbation from one set of data can be an alternative solution.

Third, the imaging is still limited to cross-sectional images with which volumetric imaging is not feasible. This inability comes from insufficient ways to acquire two sets of intensity data with and without mechanical perturbation. To overcome this limitation, synchronizing the mechanical perturbation to the OCT acquisition needs to be implemented. This synchronization can be a solution to the second limitation in the list and it can maximize the fringe washout effect.

Chapter 5: Final approach to developing OCE

Section 5.1: Introduction to pulser-receiver driven ultrasound OCE

Chapter 5 describes the final approach to the OCE system that overcomes the drawbacks from previous OCE approaches. First, this OCE method eliminates lack of three-dimensional scanning. Second, it eliminates the requirement of multiple rescanning of the same lateral location to generate one cross-sectional image. Last, it uses a new perturbation power source and eliminating excess perturbation power. Employing a new ultrasound pulser/receiver with a new ultrasound transducer as a perturbation source, overcomes the weak perturbation power. However, excess perturbation power is not ideal for fringe washout effect, optimal perturbation power needs to be based on decreasing signal at saturation of signal level itself. By utilizing the OCT acquisition trigger to ultrasound pulser/receiver control between alternating a-lines, this method made the OCE system capable of acquiring data with and without perturbation from a same image. For the perturbation power, utilizing the high-power ultrasound pulser optimizes the fringe washout effect.

The previous OCE approaches had limitation on acquiring 3D volumetric images. Our final approach to the fringe washout based OCE technique is capable of acquiring OCE volumetric images by sending short pulses of ultrasound perturbation during the acquisition of alternating depth profiles. This allows to extract cross-sectional mechanical assessment of tissue through simple comparison of the intensity in alternating pairs of depth profiles, in order to determine the amount of ultrasound-induced fringe washout. This OCE approach overcomes the drawbacks from the previous OCE approaches. First,

by eliminating the possibility of motion artifact and reducing the time between acquisition of depth profiles with and without mechanical perturbation. Second, this method does not require the same level of re-scanning of one lateral location necessary in stricter requirements for phase stability [33]. Lastly, using a new mechanical perturbation source would eliminate the weak or excess perturbation power problem.

Section 5.1.1: Pulser-receiver driven ultrasound OCE apparatus

The new approach employed an ultrasound pulser-receiver as a mechanical perturbation source in order to overcome the weak and excess perturbation power disadvantage from the previous approaches. The ultrasound stimulation was controlled using a square wave pulser-receiver (Olympus 5007PR, 400 V maximum pulse voltage) with one transducer (Olympus V318-SM, 0.5 MHz, 0.75" diameter). The pulser-receiver is capable of impulse waveforms with a possible rise in time from 10-20 ns and a maximum repetition rate of 5kHz. Figure 5.1 shows the new ultrasound has optimal perturbation power compared to the previous techniques. The receiving pulse was compared to the voltage scale measured with an oscilloscope in order to quantify the perturbation power. Figure 5.1 shows that the pulser/receiver ultrasound apparatus has superior perturbation power compared to first ultrasound approach, but it provides less excess power compared to shock wave.

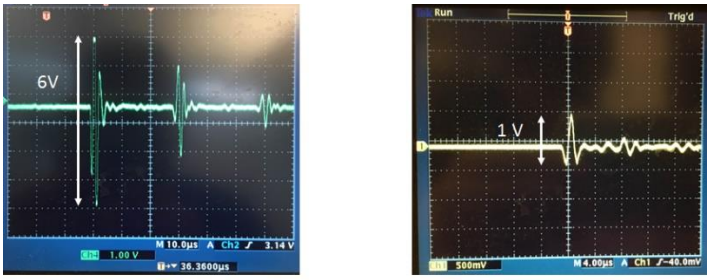

Ultrasound pulse with pulser-receiver

Ultrasound pulse with function generator

Figure 5.1 Comparison of perturbation power of ultrasound driven by a function generator and ultrasound driven by a pulser-receiver with the same transducer.

To overcome the 3D scanning limitation, the synchronizing between OCT data acquisition and ultrasound perturbation must be achieved. This synchronization makes the OCE system possible of acquiring depth profiles with and without mechanical perturbation from one image frame. To introduce the synchronization, both software and hardware must be modified. In software modification, a line trigger pulse used to synchronize the acquisition on the two line-scan camera is modified to set the line trigger sent every alternating depth profile.

Since the maximum repetition rate of the pulser-receiver was 5kHz, the OCT system is operated at 10 kHz with an ultrasound pulse duration set to be under the acquisition time for a single depth profile (100 μs). The OCT system acquires 2048 depth profiles in a frame image and 100 frame images for 3D images. The OCT acquisition program is built and interfered with hardware by Data Acquisition (DAQ) board. The DAQ board is responsible for sending triggers to each component in the OCT system. These include CCD line cameras, sample arm galvanometers and polarization modulator. The line trigger used to synchronize acquisition of the two line-scan cameras was sent

from DAQ board into a digital delay generator (function generator Stanford 1000). The digital delay generator then sent the delayed pulse to the pulser-receiver. The delayed pulse is needed to manipulate timing of ultrasound perturbation within a depth profile. To introduce this delayed pulse, a digital delay generator is implemented between DAQ board to ultrasound pulser-receiver. The pulser-receiver finally sends the short pulse of ultrasound perturbation within every alternating depth profile through the transducer into the sample. Figure 5.2 (a) shows the overall synchronized OCE apparatus, and Figure 5.2 (b) shows the trigger synchronization from OCT acquisition triggering to the ultrasound pulse. The OCE system acquired the intensity data to calculate magnitude of fringe washout. The next section describes the optimized configuration, parameters and settings of the ultrasound apparatus.

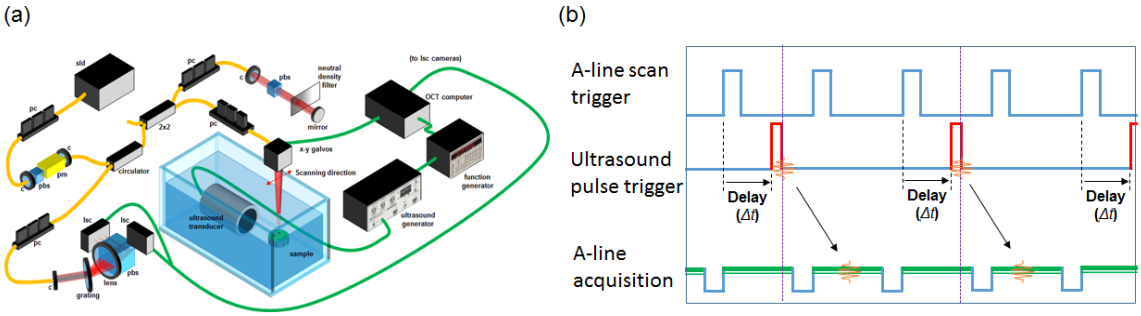

Figure 5.2 (a) Schematic of the OCE system with synchronized ultrasound perturbation system. (b) Trigger synchronization of OCE system.

Section 5.1.1.1: Post-processing

To determine the optimal parameters and settings for the OCE system, establishing the post-processing method was needed. The post-processing method of subtraction used in the previous approaches was applied however, extraction of OCT intensity information at

both with and without perturbation was needed from one image frame. As described above, the OCE system is capable of acquiring OCE images by sending short pulses of ultrasound perturbation during the acquisition of alternating depth profiles. This allows extraction of the OCT intensity values at ultrasound-induced fringe washout and without ultrasound perturbation from one image frame. The pulser-receiver was set in the way that odd numbers of depth profile had the intensity at ultrasound induced fringe washout (dB_{on}) and even numbers of depth profile had the intensity without ultrasound perturbation effect (dB_{off}), shown in Figure 5.3. Thus, the OCE images generated from the intensity difference in the dB scale ($dB_{off} - dB_{on}$) in Figure 5.3 was simply calculated by subtracting the intensity values at even depth profile numbers of 1024 depth profiles from odd depth profile numbers of 1024 depth profiles. The higher intensity difference is indicated in a red-color and the lower or zero intensity difference is indicated in a blue-color.

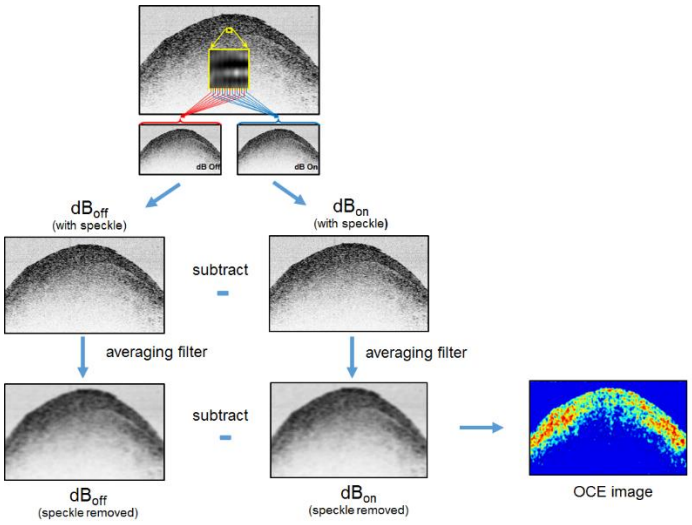

Figure 5.3 Post-processing of OCE data with depth profile separation, speckle reduction and area comparison.

Section 5.1.1.2: Ultrasound perturbation angle

One of the parameters needed to be optimized in order to maximize the fringe washout was the ultrasound perturbation angle. Figure 5.4 (a) shows the perturbation angle relative to a scanning sample and OCT sample arm. If the OCT scanning was in one direction, the ultrasound perturbation was perpendicular to the scanning line. An ultrasound transducer was placed in the water chamber at different angles to the sample shown in Figure 5.4 (b) in order to determine the optimal probe angle that provided the maximum fringe washout effect.

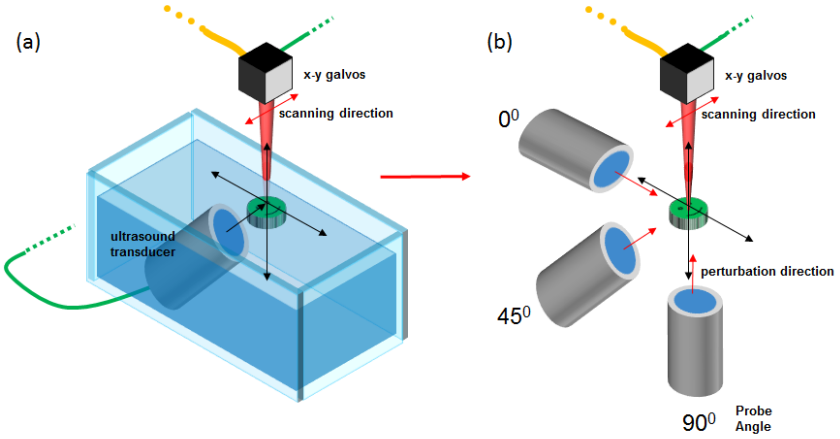

Figure 5.4 (a) Ultrasound perturbation angle α and the scanning direction. (d) difference perturbation angle α to scanning direction.

According to Yun S.H. [11], mechanical perturbation inducing axial motion to scatterers in tissue causes more fringe washout in OCT depth profile acquisition than transverse motion does. The magnitude of fringe washout was quantified by calculating the intensity difference values for each probe angle. For this probe angle study, 2% intralipid agar sample was prepared with 2g of agar (Fisher Scientific BP1423-500) resolved in 100ml

of distilled water and adding an intralipid of 2% homogeneous solution. Figure 5.5 shows the result from the probe angle study.

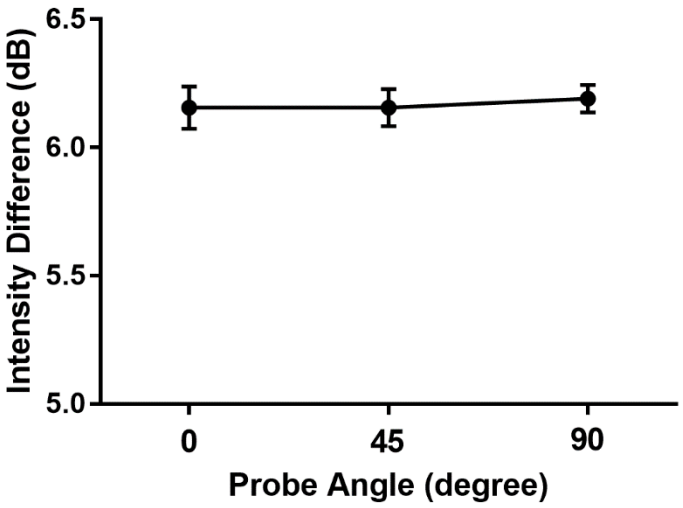

Figure 5.5 Calculated intensity difference for each probe angle (perturbation angle) α.

The result indicated that there is very little difference in intensity difference values. Thus, the probe angle could be placed in any angles ranging from 0 to 90 degrees. For our experiment, the probe angle was set to 0 degree to accommodate a biological tissue and a OCT sample arm scanning with ultrasound while considering the stability of the ultrasound transducer probe.

Section 5.1.1.3: Ultrasound pulse timing

Although the OCE system is synchronized to send a short pulse of ultrasound perturbation during every alternating depth profile acquisition, the distance between ultrasound transducer and the sample introduces a variable ultrasound pulse delay within

a depth profile shown in Figure 5.6 (a). The delay must be compensated to insure mechanical stimulation is maximally confined to within just one depth profile acquisition. To avoid this variable delay, the relative distance between the transducer and the sampling area was fixed to 40 mm shown in Figure 5.6 (b) in order to maximize the magnitude of the dB difference measured between alternating depth profiles. The distance of 40mm was considered to minimize the attenuation of ultrasound stimulation power over the distance of the ultrasound transducer to not interfere the OCT scanning. The proper ultrasound pulse delay within a depth profile was determined to provide maximum intensity difference acquired with OCE system. Figure 5.6 (c) shows the calculated intensity difference over the different ultrasound pulse delay Δt with in a depth profile acquisition. For this specific setup, the time delay was set to (20 μs) for the maximum intensity difference.

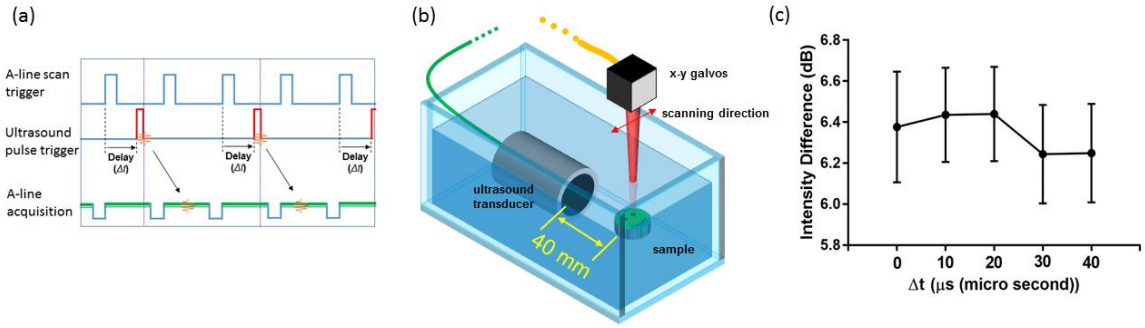

Figure 5.6 (a) pulse delay time Δt. (b) The distance between ultrasound probe and a sample set to 40 mm. (c) Calculated intensity difference for each Δt.

Section 5.1.2: Characterization of OCE with tissue phantom study

The tissue phantom study was carried with agar samples prepared in the same manner. The agar densities were prepared as 10g of the agar resolved in 100mL of distilled water

providing a 10% density. An intralipid 2% homogeneous solution was also added to the samples as scatterers. The 2%, 4%, 6%, 8% and 10% density agar samples were used to replicate the stiffness difference in biological tissues. The OCE system acquired depth profiles of agar samples containing of OCE information of ultrasound-induced fringe washout and without ultrasound perturbation information. The agar samples were imaged at pre-determined setting and parameters for ultrasound perturbation and OCT system process. The OCT system setting was a 10kHz acquisition rate composing 2048 a-lines with an imaging size to be 6mm x 2mm. The ultrasound was set to a repletion rate of 5 kHz perturbation to the sample at the transducer probe angle α at 0 degree, 40 mm away from the sample and Δt to be 20 μs. The ultrasound perturbation was set to odd depth profile numbers in order to acquire the ultrasound-induced fringe washout intensity and at even depth profile numbers to acquire the intensity without the ultrasound perturbation effect. The intensity difference in dB scale ($dB_{off} - dB_{on}$) values were calculated as described in the post-processing section for each specific area of the agar sample by subtracting the intensity values at even depth profile numbers from odd depth profile numbers.

Based on the intensity difference calculation, the heat map of the agar shown in Figure 5.7 (a) is generated. Figure 5.7 (b) shows the plot of intensity difference values at different density agar samples. The AFM strain analysis was demonstrated to verify the mechanical property of the same agar samples at the same region. The results were shown in Young's Modulus values. Figure 5.7 (c) shows the Young's modulus values for the agar samples. Figure 5.7 (d) shows the combined plot of the intensity difference

values and the Young's Modulus values that are from Figure 5.7 (b) and (c). First 5 points from left side of Figure 5.7 (d) indicate the calculated intensity difference and corresponding Young's Modulus values of agar samples. Figure 5.7 (d) illustrates the strong correlation between the magnitude of fringe washout effect quantified in the intensity difference in dB scale to the Young's modulus values from the agar samples. The results from FIGURE (d) shows that the correlation between the mechanical property and the intensity difference can be stated that stiffer the agar samples have lower intensity.

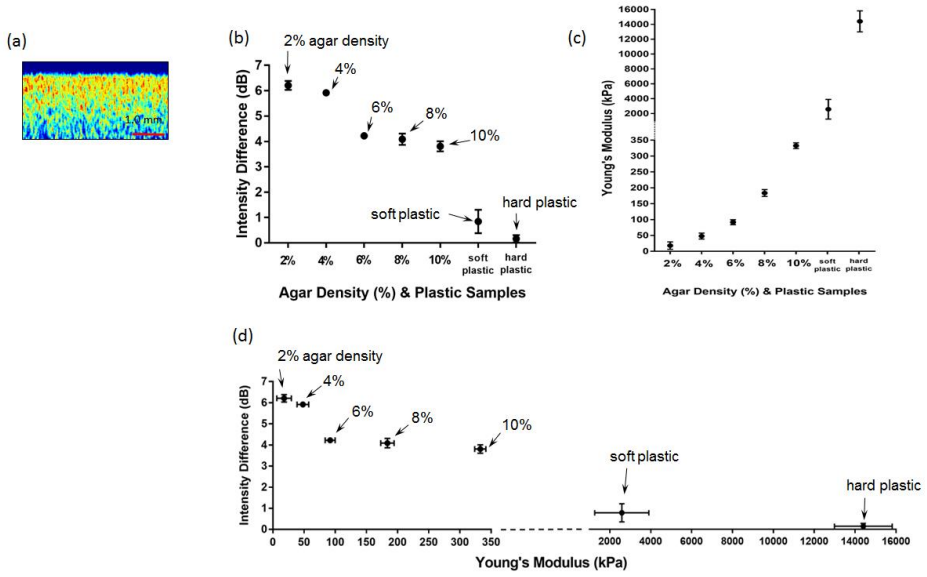

Figure 5.7 (a) OCE image of an agar sample. (b) Calculated intensity difference for each sample. (c) Measured Young's modulus for each sample. (d) Calculated intensity difference for each sample compared to measured Young's modulus for each agar density.

Section 5.1.3: Characterization of OCE with plastic samples

The variation in intensity due to fully developed coherent speckle is of the same order of magnitude as the OCT signal itself [48, 49]. However, it is expected that the magnitude of tissue motion caused by the relatively low power of the ultrasound transducer is

insufficient to significantly alter the speckle pattern between consecutive depth profile acquisitions. While we expect any remaining artifact to be significantly reduced by simple averaging with a kernel larger than the size of a speckle grain, characterization of the spatial resolution, mechanical assessment sensitivity, and requisite OCT signal level for reliable detection of an OCE signal will be performed using plastic phantoms in addition to the agar phantom study. The last two points on the right side of Figure 5.7 (d) illustrates preliminary testing on two different plastic samples which have similar Young's Modulus values to MIA model cartilages. The intensity difference derived from OCE images demonstrates a clear correlation with the Young's modulus of the samples, and spans the range for human articular cartilage [56].

Section 5.1.4: Visualization of agar sphere

This intralipid study was carried to prove that our OCE assessment is not a coincidental result from the intensity variety used in the samples caused by speckle effect in scatterers. This study tests the capability of our OCE technique and can distinguish between different mechanical properties within a sample, despite the sample having consistent intensity level and with a small sample size. We use a intralipid agar sphere (800 μm) having the similar OCT intensity level and placed it in the similar intensity level media. Both the agar sphere and media have different densities that have 8% and 2% in density respectively. Figure 5.8 (a) shows the OCT intensity image (3mm x 2mm) of the intralipid agar sphere media. The sphere boundary is hardly identified by observing in the intensity image. Figure 5.8 (b) shows the heat map image of intensity difference from the

same sample area after the application of the OCE technique. The heat map was generated in the way that higher intensity difference area is in red-color and low intensity difference area in blue-color. According to the previous tissue phantom study, the higher density region (the agar sphere) has low intensity difference and the low density region (the media) has high intensity difference. The shape of the sphere is clearly distinguished from its media in that mechanical properties of the agar sphere is much stiffer compared to its surrounding. Since this OCE technique can acquire volumetric images by synchronizing the ultrasound perturbation pulse to OCT depth profile acquisition, OCE volumetric images can be generated. Figure 5.8 (c) shows an OCE cross-sectional image in a volumetric intensity image identifying the location of an agar sphere. Figure 5.8 shows a OCE volumetric image of the agar sphere sample. This result strongly verifies our OCE technique is not a result of coherent speckle patterns. The OCE technique can acquire OCE volumetric images to identify unknown mechanical properties.

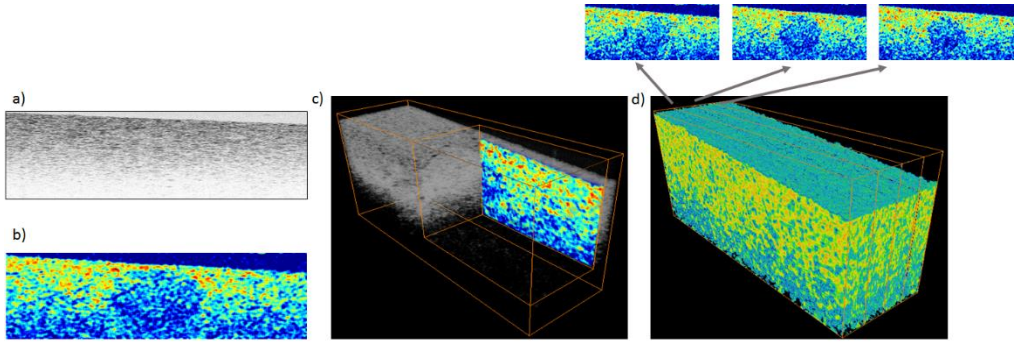

Figure 5.8 The OCT intensity cross-sectional image of the agar sphere. (b) The OCE cross-sectional image of the agar sphere. (c) The OCE cross-sectional image of the agar sphere shown in the OCT intensity volumetric image. (d) The OCE volumetric image with the OCE image frames shown above.

Section 5.2: *In vitro* study with arthritis induced rat cartilage with OCE

The other batch of MIA-day0 and MIA-day11 cartilages were imaged with the OCE technique. The cartilages were imaged in the same manner described in Figure 5.2. The same OCE analysis described in post-processing was applied to calculate the intensity difference and to generate the heat maps. Since this OCE technique can send a short pulse of ultrasound during acquisition of every alternating depth profile, it is capable of acquiring the 3D image instead of just a cross-sectional image alone. Figure 5.9 (a-1), (a-2), (a-3), (b-1), (b-2) and (b-3) show an OCE cross-sectional image in an intensity 3D image. Figure 5.9 (a-1), (a-2) and (a-3) are images of MIA-day 0 cartilage and Figure 5.9 (b-1), (b-2) and (b-3) are images of MIA-day11 cartilage. Comparing two OCE cross-sectional images from MIA-day0 and MIA-day11, the progression of OA can be identified by the amount of intensity difference appearing on the OCE images. Figure 5.9 (a-1), (a-2), and (a-3) clearly show more intensity difference region than Figure 5.9 (b-1), (b-2) and (b-3) show. The right side of Figure 5.9 shows the full OCE 3D images of MIA-day0 and MIA-day11 with OCE cross-sectional images taking out from sections of 3D images shown above. This verifies the full capability of the OCE technique to scan, acquire and analyze 3D images. These intensity difference can also be determined by simply calculating the average intensity difference as a function of depth for each cross-sectional image. The plot shown in Figure 5.10 indicates the intensity difference values for MIA-day0 and MIA-day11 cartilages. The comparison of intensity difference values, MIA-day0 has much higher intensity difference compared to MIA-day11. Also, MIA-day11 average intensity difference plot shows the shallow depth that the intensity

difference can be only observed up to 150 depth points (585μm) compared to MIA-day0 with 250 depth points (980μm).

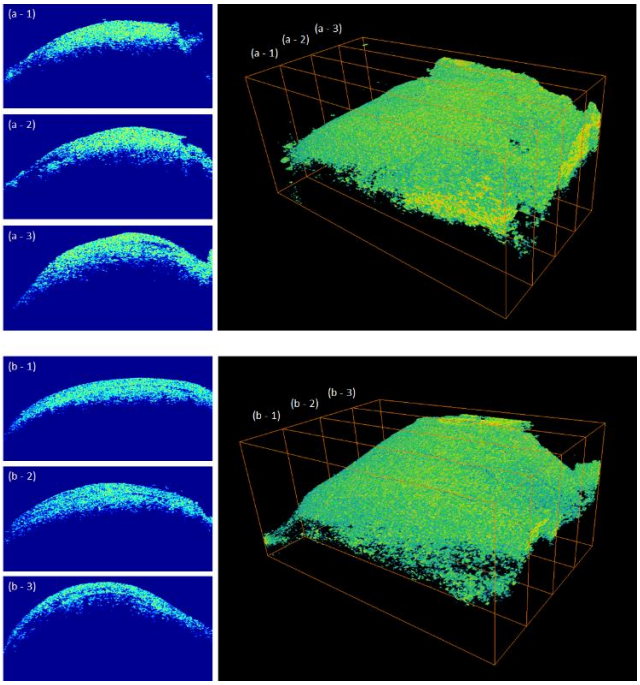

Figure 5. 9 (a – 1) (a –2) (a – 3) the OCE cross-sectional images of the OCE volumetric image at the different locations for MIA-day 0 knee sample. (b – 1) (b – 2) (b – 3) the OCE cross-sectional images of the OCE volumetric image at the different locations for MIA-day 11 knee sample.

These intensity difference can also be determined by simply calculating the average intensity difference as a function of depth for each cross-sectional image. The plot shown in Figure 5.10 indicates the intensity difference values from one set of cross-sectional image for MIA-day0 and MIA-day11 cartilages. The comparison of intensity difference values, MIA-day0 has much higher intensity difference compared to MIA-day11. Also, MIA-day11 average intensity difference plot shows the shallow depth that the intensity difference can be only observed up to 600μm compared to MIA-day0 with 850μm.

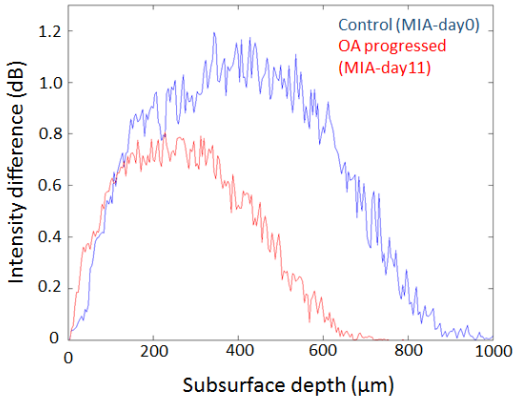

Figure 5.10 Average intensity difference as a function of depth for an cross-sectional image.

Section 5.3: Conclusion

In chapter 5, we focused on developing a fringe washout based OCE system capable of acquiring volumetric images. Volumetric imaging was achieved by sending short pulses of ultrasound during the acquisition of alternating depth profiles. Ultrasound perturbation and OCT depth profile acquisition were synchronized throughout volumetric imaging of samples. This allowed to extract the intensity at both ultrasound-induced fringe washout and non-ultrasound perturbated from one image frame. This OCE approach eliminated the possible motion artifact by reducing the time between acquisition of depth profiles with and without ultrasound perturbation. The approach also eliminated the requirement of the same level of re-scanning on one lateral location necessary for phase stability.

The capability of this OCE approach was tested and verified through the tissue phantom study and the *in vitro* study. In the tissue phantom study, variable density agar samples were utilized to test the detection of the OCE technique. The intensity difference values and corresponding Young's Modulus values verified that the intensity difference

has of stiffer the agar sample (10%) with a higher intensity difference (< 4 dB). The new ultrasound setup has sufficient perturbation power and eliminated the weak or excess perturbation power problems from the previous approaches. Since there is not limitation on available ultrasound perturbation pulses, we were able to conduct much characterization with different samples. Two plastic samples were utilized to replicate the stiffness of knee samples. The stiffness was verified by calculating the Young's Modulus values of each sample compared to the MIA-model cartilages. The corresponding intensity difference values of plastic samples verified that the detection of the intensity difference was not the remaining of insufficiently reduced speckle patterns. This was also verified through the agar sphere study. Although the intensity level is similar throughout the sample, the OCE image was able to distinguish the agar sphere from the surrounding media. This proves that the OCE technique has a reliable detection of mechanical properties.

In *in vitro* study, the OCE method was capable of imaging volumetric images. This has an advantage in detecting mechanical property changes that could occur throughout the knee cartilage during random stages. The MIA model study proved the OCE method is sensitive enough to detect the small mechanical property changes in knee cartilage, these results clearly indicate MIA-Day11 cartilage has greater mechanical stiffness compared to the control model. The results highlighted that the synchronized ultrasound induced fringe washout based OCE is a potential elastography technique.

Chapter 6: Conclusion and future studies

Section 6.1: Conclusion for OCE studies

In summary, the work presented in this dissertation describes the use of OCT for elastography. OCT imaging technique applied to elstography is known as optical coherence elastography (OCE). The advantage of OCE technique is to provide distinct higher spatial resolution and higher magnitude features compared to ultrasound and magnetic resonance elastography. OCE is commonly used to detect small mechanical property changes in tissue. OCE technique is not a new invention; however, an OCE technique based on fringe washout effect is a new invention which overcomes the disadvantages of the previous OCE methods such as limited imaging region and intensive computation. This high spatial resolution OCE technique can be applied to a common disease such as osteoarthritis (OA). OA is an evasive disease that common imaging modalities cannot detect at the early stage. OCE can detect the mechanical property changes of OA during the effective therapeutic window of opportunity.

The method of fringe washout base OCE relies on quantifying the decrease of OCT intensity signal by comparing the intensity level with and without external perturbation. This decreased intensity signal can be directly related to the perturbation induced displacement of scatterers in the tissue. Thus, the tissue is either dense or stiff, the displacement of scatterers responds to a given acoustic power being smaller where decreases of intensity caused by fringe washout is smaller.

In Chapter 3, the results were presented to provide the proof of concept of the OCE method. The first approach utilized an ultrasound perturbation driven by a function

generator. The tissue phantom study was conducted using different density agar samples to replicate tissue stiffness. The intensity difference in the dB scale was calculated to assess the stiffness of the samples. The results of calculated intensity difference for each agar sample was verified with the results from AFM measurement of Young's modulus, where a sample with higher Young's modulus value had lower intensity difference value. The expected results were that the amount of intensity difference was closely related to the measured Young's modulus. The *in vitro* study was conducted to provide the realistic application of this OCE method. The results of intensity difference calculation on MIA induced osteoarthritis progression models showed close characteristic to the tissue phantom study. The negative aspect of this first approach was the weak perturbation power insufficient to cause proper amount of fringe washout effect.

In Chapter 4, the use of shock wave was determined to be a replacement of higher perturbation power. Unfortunately, limited access to the shock wave pulse generator was allowed to this OCE application. A similar experimental method was applied during the tissue phantom study that shows the sample with higher Young's modulus value had lower intensity difference value. In this approach, there were few improvements on OCE analysis. First the OCE cross-sectional images were generated. This was an additional capability to the OCE technique showing the clear deformation of samples can be visualized. For the OCE images on MIA models, the red-lines indicated the boundary between lower intensity difference and higher intensity difference based on the calculated threshold in depth locations. The results showed the characteristic of OA where the knee cartilage was calcified as in OA progression. Second, a detailed analysis was applied to

MIA models in the sampling locations where calculations of intensity difference and measurements of Young's modulus were correlated. The results show that both intensity difference and Young's modulus values from the same location within the MIA knee were closely related. The negative aspects were excessive perturbation power and incapability of acquiring volumetric images.

Since generating the OCE images was achieved, the technique to acquire volumetric images on samples was explored in Chapter 5. The acquisition of OCE volumetric image was achieved by synchronizing the ultrasound perturbation to the OCT depth profile acquisition. This synchronization also solved the problem of requiring multiple rescanning of same lateral locations. The OCE technique can extract the OCT intensity information with and without ultrasound induced fringe washout with the use of simple comparison of the intensity in alternating pairs of depth profiles. The experimental method was thoroughly considered in the detailed characterization of new ultrasound pulser-receiver accomplished. The parameters of the OCE system were optimized to provide efficient fringe effect in the ultrasound perturbation angle, the distance between the ultrasound to samples, and the pulse time delay. In addition to the basic tissue phantom study and *in vitro* study, the agar sphere model, birefringence study (shown in Chapter 6) and depth limitation study were conducted to truly indicate the capability of this OCE system. The post-processing method was also optimized to generate enhanced OCE images by altering the intensity difference calculation equation.

In conclusion, our OCE technique based on the fringe washout effect induced by mechanical perturbation is capable of detecting small mechanical property changes in

biological samples. Although our OCE method is not as sensitive as other OCE methods such as speckle tracking, phase-sensitive detection and Doppler spectrum detection, the OCE method is considerably more efficient as it requires little hardware modification and computationally efficient compared to the existing OCE system. By implementing the ultrasound pulse trigger control, the OCE method is capable of imaging in 3D volumetric images. This has an advantage in detecting mechanical property changes that could occur throughout the knee cartilage during random stages of OA. The MIA model study proves that the OCE method is sensitive enough to detect the small mechanical property changes in knee cartilage and the results clearly indicates MIA Day11 cartilage has greater mechanical stiffness compared to the control model.

Further study needs to be demonstrated for greater understanding of this OCE method. Further work will include applications of our OCE method to MIA model with different time points. The time points will be earlier or later stage of OA progression beyond what this experiment has explored. This will ensure the sensitivity of our OCE methods to detect the progression of OA. The different rat model needs to be tested with this OCE method. The true utility of our imaging technique would be better demonstrated in an OA model that is caused by a traumatic injury [57-59] since post-traumatic osteoarthritis (PTOA) is a common form of arthritis. A patellofemoral joint impact trauma model will be utilized to induce PTOA in rats. While the MIA model used in the preliminary studies is highly predictable and well characterized, cartilage damage and its progression does not depict those of PTOA [60]. Thus, the true utility of the OCE

technique would be better demonstrated in an animal model that induces arthroscopically undetectable subsurface cartilage dames.

One of the advantages of fiber-based SD-OCT is having polarization-sensitive OCT (PS-OCT) function. PS-OCT can detect and quantify localized changes in collagen by assessing birefringence of collagen [33, 61-77]. Our hypothesis is that a combination of OCE with quantitative polarization-sensitive OCT (PS-OCT) will provide a means to non-destructively assessment of glycosaminoglycan (GAG), one of the earliest changes observed in cartilage of early OA [28, 29]. The mechanical properties of cartilage measured by OCE is derived from the density and organization of both collagen and glycosaminoglycan (GAG), while birefringence from PS-OCT arises primarily from collagen, a combination of OCE and PS-OCT should be possible to make quantitative assessment of GAG alone. The preliminary results of this PS-OCT study of GAG is described later in Chapter 6.

Successful completion of this project will lead to the development of arthroscopic OCT by utilizing fiber optics in combination with a clinical ultrasound system, and enabling translational applications of the developed technology. This choice is further justified by the fact that the clinical standard for care in a traumatic joint injury involves arthroscopy. A number of studies have demonstrated the ability to implement optical coherence tomography endoscopically [78]. In Chapter 6, the preliminary results of developing arthroscopic OCT is demonstrated.

Section 6.2: PS-OCT preliminary study

A portion of the further study mentioned in Section 6.1 have been achieved to show the future of the OCE study. A further study is to provide a means for non-destructively assessment of glycosaminoglycan (GAG), one of the earliest changes observed in cartilage of early OA [28, 29].

The multi-functional properties of the OCT system allow for simultaneous visualization of intensity and polarization-sensitive OCT (PS-OCT) imaging by passing the light from both arms through a fiber splitter and circulator, and then directing it to a polarization-sensitive spectrometer [66, 67, 79]. In the spectrometer, the light is split by a polarizing beam splitter cube and projected onto two line scan cameras. PS-OCT uses depth-dependent changes in the polarization states of light returning from within a sample to determine the light polarization changing properties of a sample [64, 80]. The main property that occurs in biological tissue is birefringence. Birefringence is the optical property where the refractive indices are different along the two orthogonal polarization components of light. The two polarization components of light propagate at a different speed in a birefringent material caused by difference in refractive indices [64]. Thus, a phase retardation is generated between the two polarization states. Assuming a difference in refractive index is Δn, the two beams of wavelength λ will experience a cumulative phase retardation η, and Δz as the distance of light traveled through the birefringent material that gives $\eta = 2\pi \Delta n \Delta z / \lambda$ [81]. This phase retardation leads to an alteration of the resultant polarization state of the wave. Depth resolved maps of phase retardation can be analyzed to quantitatively determine birefringence. A number of biological samples

exhibit birefringence in the amount which can be attributed to a combination of density and organization of fibrous structures.

PS-OCT imaging and data analysis were performed in the following manner. Corresponding MIA model cartilages were imaged in an orientation that the scanning axis of the sample beam was parallel to the medial line shown in Figure 6.4.

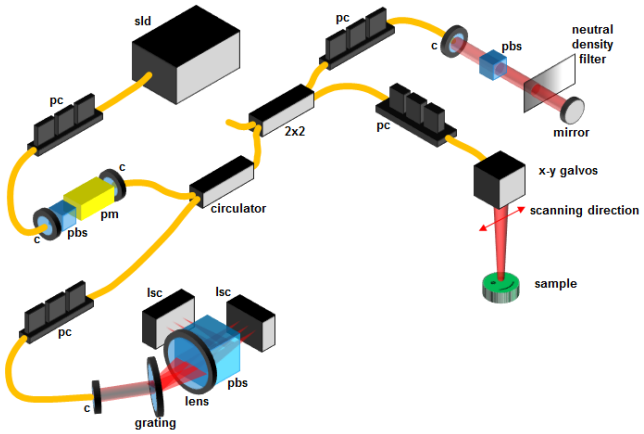

Figure 6. 1 Schematic of PS-OCT system

This imaging orientation provides cross-sectional images composed of 2048 depth profiles with 4.0 mm scanning range with 2 mm imaging depth. A sequence of 100 such images was acquired. Birefringence of cartilage was detected in PS-OCT by depth-dependent changes in the cumulative phase retardation experienced by different polarization states of the reflected light. The rapid changes in phase retardation and polarization state of cartilage were detected as increasing in its birefringence. The rate of the depth-resolved change in phase retardation was proportional to the birefringence of the cartilage. The cumulative phase retardation was expressed as angle of a gray scale from black (0^o) to white (180^o). These angles were used to construct and display all possible polarization states of light in PS-OCT. The birefringence of cartilage was

quantified in slope by plotting the phase retardation angle over depth of sampling region shown in Figure 6.2. Phase retardation as a function of depth was averaged for the central 50% of cartilage region in each frame. Each obtained slope for each frame in a data set was averaged.

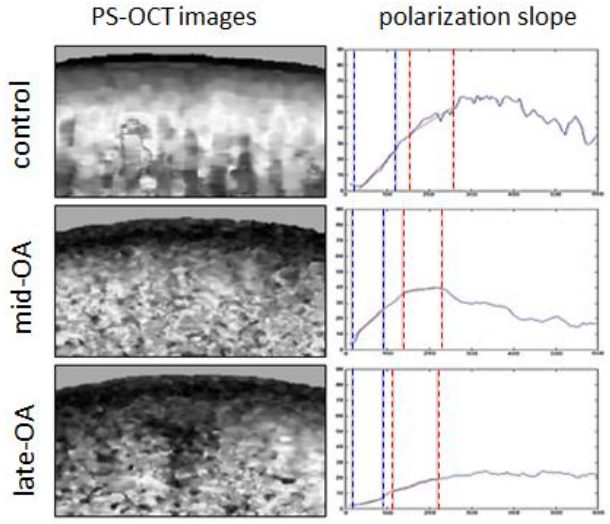

Figure 6. 2 PS-OCT images of MIA model cartilages and corresponding phase retardation as a function of depth

Figure 6.2 shows histology images, OCT intensity images, plot of depth dependent intensity change, PS-OCT images, and plot of phase retardation as a function of depth for each cartilage sample from MIA-day 0, MIA-day 5 and MIA-day 11. PS-OCT images visualized birefringence which is the optical property indicating the changes in the refractive indices of cartilage. Since MIA injection denatured the collagen organization, its fibrous structures and density, birefringence significantly indicated the changes of its refractive indices [82]. The phase retardation plots in Figure 6.2 shows the cumulative phase retardation as a function of sub-surface depth. The slope in red indicates the degree of birefringence for each sample. The slope quantified the denaturation of cartilage that

the slope values decreased as OA progresses. For further study, comparison between the phase retardation slope values and histomorphological measurements is needed to establish the relation between slopes. The slopes for control, MIA-day5 and MIA-day11 are 0.2468, 0.1835, and 0.0766^{o}/μm respectively.

Since the mechanical properties of cartilage derive from the density and organization of both collagen and GAG content while optical birefringence from PS-OCT arises primarily from collagen, the combination of OCE and PS-OCT techniques should be possible to make quantitative assessment of GAG alone from two sets of information. To better demonstrate the additional contrast provided by OCE, a sample of cartilage was placed under a thin layer of chicken breast tissue and imaged with OCE and PS-OCT systems. As shown in Figure 6.3, the border between the muscle and cartilage layers is clearly evident in the OCE image, but it is difficult to identify with PS-OCT.

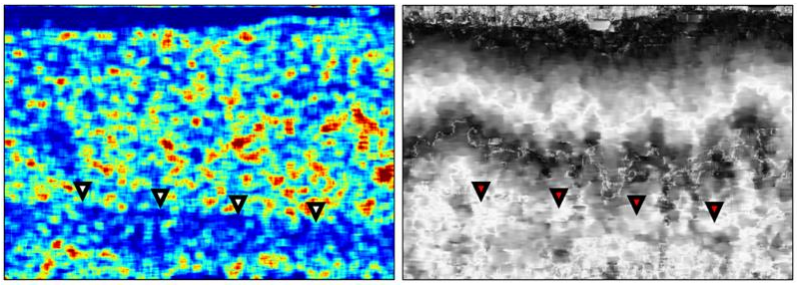

Figure 6.3 OCE (left) and PS-OCT (right) images of cartilage under a thin layer of chicken muscle. The border between the two different tissues is indicated by the triangles.

Section 6.3: Forward-viewing endoscope for arthroscopic OCT

OCT is a promising technique for clinical imaging that is capable of high-resolution of cross-sectional imaging endogenously [1]. Although OCT fulfills the gap between more traditional optical imaging methods, such as confocal microscopy and

medical imaging techniques such as ultrasound and magnetic resonance imaging, the imaging penetration depth of OCT is typically limited to a few millimeters. OCT cannot visualize structures located deeper in tissue; the only way to gain access to the surface of a particular tissue is to surgically expose the regions that we have demonstrated in *in vitro* study with MIA knee cartilage models. Previous studies have shown that OCT can circumvent these limitations with endoscopic sample arms [83-90]. Most of the OCT endoscopes work as a needle base penetration that can view the forward or side as the needle endoscope penetrates [83-90]. An OCT-adapted needle endoscope makes it feasible to reach the local area in a minimally invasive manner [91].

Few studies show the implementation of gradient-index (GRIN) lens technology where GRIN lens is placed into the tip of needle connected to a single optical fiber for a biopsy known as an OCT-adapted fine needle aspiration (FNA) probe [90]. This technique is capable of giving a single depth profile scan (A-line scan) that is intensity as a function of depth. This needle endoscope is capable of identifying various tissue types such as adipose, fibrous, and tumor with over 80% specificity by an automated algorithm where sensitivity was demonstrated from single intensity depth profiles. The only downside of this endoscope is the ability to only provide a single depth profile further limiting the optical scanning range of OCT endoscopes.

Previous studies have demonstrated the wider scanning range of OCT endoscope. The side-viewing OCT endoscope captures the images of side walls for cardiac [92, 93] and gastroenterological imaging [94, 95] through volumetric imaging endoscopes. This can be achieved with the feature of the side wall of tunnel like tube imaging samples of

endoscopes. The other endoscopes known as forward-viewing OCT endoscopes capture images of what exists in front of it. The forward-viewing OCT endoscopes have restricted their clinical use [83-90] due to few disadvantages. A paired-angle-rotation scanning (PARS) OCT forward imaging probe is designed to utilize a pair of angle-cut rotating GRIN lenses to deflect and scan the OCT probe beam across the forward region ahead of the probe tip [89]. These two GRIN lenses are placed in two different needles which are rotated equal and opposite angular speed and directions to acquire multiple depth profiles. This technology is claimed to have volumetric scan (3D scan), but its actual physical implementation is not robust. The non-uniformity patterns of sampling density throughout the field of view is the main disadvantage because the center part has much higher sampling density than the peripheral region.

The purpose of this work aims to develop a handheld, lightweight and robust forward-viewing OCT endoscope that addresses previous shortcomings, and to demonstrate the potential of this endoscope used in OCE system that can be minimally invasive to assess damage on cartilage for early OA stage detection. Implementation of the endoscope to the existing OCE system is feasible since our OCT is based on optical fiber-based implementation. This fiber-base OCT facilitates flexible system configuration as difference components can easily be exchanged. This feature is particularly useful when the sample arm optics need to be interchangeable or disposable.

Few preliminary versions of the endoscope have been developed. Figure 6.3 shows the first prototype of the forward-viewing endoscope.

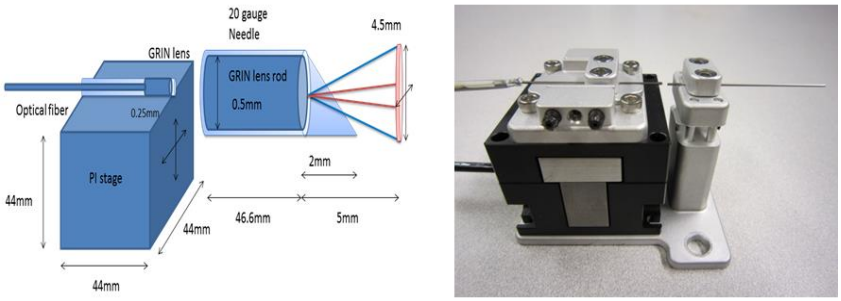

Figure 6.4 Schematic of first prototype of forward-viewing endoscope and a picture of built prototype.

Developing this endoscope began with assembling the scanning apparatus shown in Figure 6.1. A gradient index (GRIN) objective lens (GRINTECH 0.25mm diameter, 0.57mm length, 1.635 Reflective index with 5 mm working distance) was affixed to the end of a single mode optical fiber (Thorlabs SM FC/APC 9.2 µm diameter) using an UV curable optical adhesive. This assembling had to be completed carefully to minimize the internal reflection of light on the interface between the GRIN lens and the optical fiber and to obtain the maximum beam power achieved at the end of GRIN lens. Constantly checking with a power-meter placed at the end of the GRIN lens for obtaining the maximum light beam power while monitoring the characteristic and minimizing the internal reflection on the OCT spectrum by plugging the optical fiber to the sample arm of OCT system. Assembly of the GRIN lens to the optical fiber was secured by affixing it in a stainless steel outer shield (CANDENCE 22 Ga.). The second part was to assemble the needle apparatus which penetrates into to the sample tissues shown in Figure 6.3. The GRIN endoscopic rod lens system (GRINTECH 0.5mm in diameter and 46.6mm in length) was affixed into a 20 gauge needle by thermal adhesive.

The piezoelectric stage (P-611.3 NanoCube XY Piezo Stage) from the PI was used in this prototype. This cubic stage (44 mm x 44 mm x 44 mm) could move in x-y directions corresponding to the light beam path axis powered by piezoelectric technique to applied voltages. The scanning apparatus and the needle apparatus were affixed on to the PI stage by the machine fabricated stage shown in Figure 6.1. The area of scanning and working distance (focal point) of endoscope were manipulated depending on displacement of the scanning apparatus to the GRIN lens needle apparatus. The ideal working distance of this endoscope was three millimeters in vivo and area scan to be one millimeter wide. Scanning of large displacements might have caused unwanted noise and field curvature which could be minimized by alignment and characterization. This endoscope was precisely synchronized to the acquisition program on our OCT system written in C++ code. Using the PI stage introduced very high mechanical vibration caused by frequent movement of the PI stage in x and y directions. This generated vibration was high and caused destruction of the light beam relay between the scanning GRIN lens to the GRIN lens rod. This destruction caused a jitter in the OCT image resulting in unclear images at edges of samples.

In order to overcome this high mechanical vibration in this endoscope, modification of the PI scanning stage with a miniaturized galvanometer mirrors assembled with two gold spatter-coated piezoelectric bending actuators was required as shown in Figure 6.4.

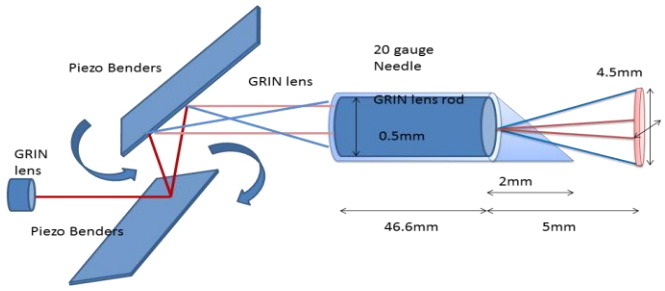

Figure 6.5 Schematic of piezoelectric bending actuators.

This technique would minimize the mechanical vibration and making it more similar to the common galvanometer sample arms. However, the gold spatter-coating directly applied on the piezoelectric bending actuators did not provide the laser reflectivity desired. It resulted in only 60% of the laser beam reflection after two actuators. Also, the actuators did not provide the same plane scanning capability, making the pivot point of the actuator not centered. The common commercialized galvanometers are made to scan in the same plane and distance between the imaging field to the galvanometer mirror does not change over the scanning angles. An alternative solution was to replace the actuators with the common galvanometers. However, the limitation of the galvanometer mirrors were too large to be incorporated in the apparatus.

The solution to the mechanical vibration and the actuator problems was to introduce a microelectromechanical system (MEMS) mirror. MEMS utilizes electromagnetic actuators to introduce movement to a device. Thus, the micro-mirror placed on the MEMS can move three-dimensionally to introduce volumetric scanning which the raster scanning is capable of performing. Figure 6.5 (a) shows the schematic of the latest prototype of the endoscope. It consists of a MEMS mirror (Mirrorcle 4.23 x 4.23 mm, mirror diameter Ø 2.0mm, x-y tilt angle ±5^{o}), a 1310nm collimator (Thorlabs

Ø1.42mm beam waist), a fixed mirror (Thorlabs, Ø = 25.4mm), a focusing achromatic doublet lens (Thorlabs, Focal length 19.0mm, Ø = 12.7mm, Ø < 20µm beam waist), and a GRIN-lens rod (GRINTECH 50mm, Ø = 500µm). The collimator collimates the 1310nm wavelength laser beam to the face of the fixed mirror which mirror was introduced to redirect to achieve a compact configuration of endoscope. The reflected laser hits the MEMS mirror at the beam waist of the laser located under the mirror diameter (2.0mm) where it maximizes the use of MEMS mirror aperture. The laser is then focused by the focusing lens to the face of the GRIN-lens rod. The laser beam propagates to the other end of the rod and focuses at 2mm. The end of the GRIN-lens rod is shaped in a small angle (< 8^{o}) to avoid the effect of internal reflection. The GRIN lens rod is enclosed in a needle housing and other components are also placed in a housing shown in Figure 6.5 (b).

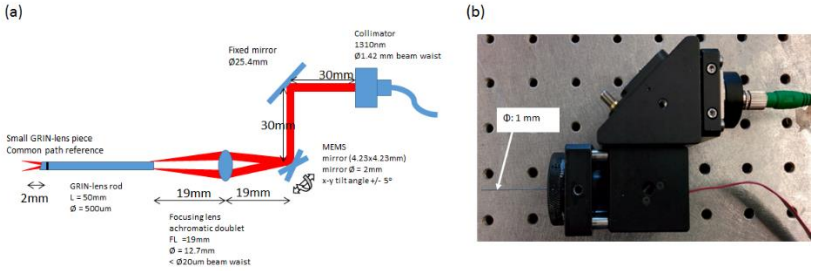

Figure 6.6 (a) schematic of an endoscope with MEMS mirror. (b) the recent prototype of the endoscope.

This prototype has significantly superior benefits making the overall device lighter in weight and less prone to alignment error. Basic characterization of the light throughput in the lateral and axial resolution, and overall stability were conducted.

Further study of this endoscope will be followed by optimization of a real-time acquisition and visualization program for rapid 3D visualization of the volume of tissue near the distal end of the needle probe. This will facilitate real-time identification of different tissue types (muscle, fat, bone, nerve, vasculature) for real-time guidance of the needle to a structure of interest. After construction of these needle sample arms, optimizing post-processing schemes is crucial for phase stabilization. The main problem here is the removal of the effects of bulk motion (e.g., breathing artifact, relative movement of the needle with respect to the sample of interest), which can be achieved with optimization of a depth-dependent intensity weighting to remove an average phase displacement related to bulk motion. These algorithms will be tested and optimized using simulated vasculature and then animal models. Successful completion of these criteria will provide critical groundwork for future translational application of minimally-invasive, high-resolution and volumetric imaging extensions in OCE system to improve assessment of biological structures.

Additional use of the endoscope in PS-OCT system as a sample arm is considered. This endoscope application could lead to minimally-invasive assessment of GAG in cartilages. The mechanical properties of cartilage measured by OCE is derived from the density and organization of both collagen and glycosaminoglycan (GAG). Birefringence from PS-OCT arises primarily from collagen, a combination of OCE and PS-OCT should be possible to make quantitative assessment of GAG alone. However, the use of the endoscope in PS-OCT may be difficult to achieve since we have not used it in vivo studies. It may require some modification of the endoscope properties for working

distance and the scanning range. These obstacles can be overcome with careful alignment and positioning of the endoscope hardware. The changes in properties of the endoscope may lead to feasible modification of software. The more difficult part is to locate the orientation of images initially that we will be observing through a forward-viewing endoscopic OCT needle probe since we don't have the preliminary study. Guiding the endoscope in biological sample is necessary for this study. Simple guiding to the cartilage target region is determined by touch. One systematic guiding is to use ultrasound imaging by roughly imaging the location and distinguish between tissues [96]. Another systematic option is to use an arthroscope described in [97] where the arthroscope is inserted in an angle to the OCT probe. The results obtaining from this endoscope study should give similar trends found in the initial studies.

Section 6.4: Side-viewing endoscope for arthroscopic OCT

Although the forward-viewing endoscope is adequate for the purpose of searching and has been in the development process, the side-viewing endoscope is suitable for this arthroscopic application purpose. As mentioned previously, the previous studies have provided evidence of side-viewing endoscope application in OCT imaging. Since the feature of the side-viewing endoscope is to image side walls of the tunnel like space, the endoscope will be inserted into femorotibial synovium via antero-medial approach without incision for imaging shown in Figure 6.6. Thus, the side-viewing endoscope will be imaging subsurface of articular cartilages in both femur and tibia.

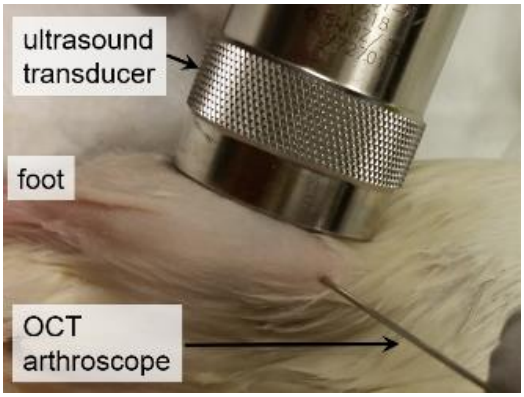

Figure 6.7 OCT endoscope (arthroscope) insertion into osteoarthritis induced rat cartilage in *in vivo* study

The side-viewing endoscope will be built with a single mode fiber, a spacer, GRIN lens, prism, an imaging windows glass and a needle shield in a 21 gauge needle housing (Ø = 500µm). All the components will be affixed to each other with optical glue for maximum light transfer as shown in Figure 6.7. The single mode fiber is affixed to a spacer which allows the optical beam to be propagate to the aperture of the GRIN lens. The GRIN lens then focuses the optical beam to focal length of a few millimeters depending on the imaging sample. The prism redirects the focusing optical beam to the 90º angle out to the imaging window which the optical beam is focused.

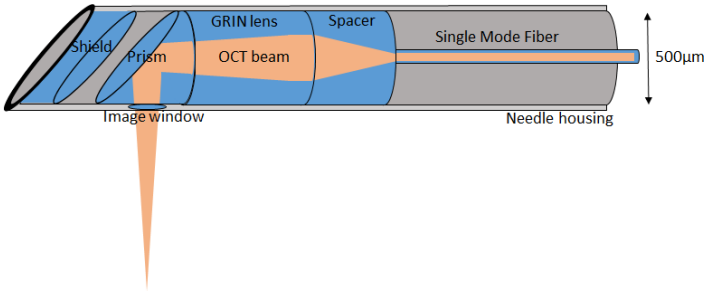

Figure 6.8 Schematic of side-viewing endoscope probe

The extensions of OCT function such as OCE and PS-OCT can be used with the endoscope. The application of the side-viewing endoscope with OCE system will be

feasible with the sample arm of OCE system can simply be exchanged to the endoscope as it is compatible with the optical fiber base OCT. The side-viewing endoscope working as an arthroscope will acquire OCE information from the target region in the knee cartilage samples, and the information will be analyzed in the same manner. PS-OCT can be used to acquire birefringence information through the endoscopic sample arm. This use of the endoscope in PS-OCT system can be difficult since the preliminary study wasn't achieved prior to this dissertation. However, the combination of the side-viewing endoscope, OCE technique and PS-OCT technique will provide a means to minimally-destructive imaging modality to assess the changes in GAG property which is the early symptom of osteoarthritis. Successful completion of this project will lead to the establishment of arthroscopic OCT by utilizing fiber optics in combination with a clinical ultrasound system, enabling translational applications of the developed technology.

Reference

1. Huang, D., et al., *Optical coherence tomography.* Science, 1991. **254**(5035): p. 1178-81.

2. Drexler W, F.J., *Optical coherence tomography: technology and applicaitons.* Springer Science & Business Media, 2008.

3. Wang, Y., *Development and Applications of 4D Real-Time Multi-Founctional Spectral-Domain Optical Coherence Tomography*, in *Bioengineering*. 2013, University of California, Riverside. p. 171.

4. Fercher, A.F., Hitzenberger, C.K., Kamp, G., and El-Zaiat, S.Y., *Measurement of intraocular distances by backscattering spectral interferometry.* Optics Communications 1995. **117**(1-2): p. 43-48.

5. Mitsui, T., *Dynamic range of optical reflectometry with spectral interferometry.* Japanese Journal of Applied Physics 1999. **38**: p. 6133-37.

6. Rodriguez, C.L., *Development and Application of Optical Coherence Tomography for Detection of Cerebral Edema In Vivo*, in *Bioengineering*. 2015, University of California, Riverside.

7. Izatt, J.A. and M.A. Choma, *Theory of Optical Coherence Tomography*. Optical Coherence Tomography: Technology and Applications, 2008: p. 47-72.

8. Ha Usler, G. and M.W. Lindner, *"Coherence radar" and "spectral radar"-new tools for dermatological diagnosis.* J Biomed Opt, 1998. **3**(1): p. 21-31.

9. Chan, K.K.H., *Spectral domain optical coherence tomography system design : sensitivity fall-off and processing speed enhancement*. 2010, The University of British Columbia.

10. Nassif, N., et al., *In vivo high-resolution video-rate spectral-domain optical coherence tomography of the human retina and optic nerve.* Opt Express, 2004. **12**(3): p. 367-76.

11. Yun, S.H., et al., *Motion artifacts in optical coherence tomography with frequency-domain ranging.* Opt Express, 2004. **12**(13): p. 2977-98.

12. Yun, S.H., et al., *Pulsed-source and swept-source spectral-domain optical coherence tomography with reduced motion artifacts.* Opt Express, 2004. **12**(23): p. 5614-24.

13. You, J.W., et al., *Pulsed illumination spectral-domain optical coherence tomography for human retinal imaging.* Opt Express, 2006. **14**(15): p. 6739-48.

14. Lawrence, R.C., et al., *Estimates of the prevalence of arthritis and other rheumatic conditions in the United States. Part II.* Arthritis Rheum, 2008. **58**(1): p. 26-35.

15. Murphy, L.B., et al., *Estimating medical costs attributable to osteoarthritis in the US population: comment on the article by Kotlarz et al.* Arthritis Rheum, 2010. **62**(8): p. 2566-7; author reply 2567-8.

16. Dahaghin, S., et al., *Prevalence and pattern of radiographic hand osteoarthritis and association with pain and disability (the Rotterdam study).* Ann Rheum Dis, 2005. **64**(5): p. 682-7.

17. Kuhn, K., et al., *Cell death in cartilage.* Osteoarthritis and Cartilage, 2004. **12**(1): p. 1-16.

18. Eckstein, F., et al., *One year change of knee cartilage morphology in the first release of participants from the Osteoarthritis Initiative progression subcohort: association with sex, body mass index, symptoms and radiographic osteoarthritis status.* Annals of the Rheumatic Diseases, 2009. **68**(5): p. 674-679.

19. Neogi, T., et al., *Cartilage Loss Occurs in the Same Subregions as Subchondral Bone Attrition: A Within-Knee Subregion-Matched Approach From the Multicenter Osteoarthritis Study.* Arthritis & Rheumatism-Arthritis Care & Research, 2009. **61**(11): p. 1539-1544.

20. Felson, D.T., et al., *Comparison of BLOKS and WORMS scoring systems part II. Longitudinal assessment of knee MRIs for osteoarthritis and suggested approach based on their performance: data from the Osteoarthritis Initiative.* Osteoarthritis and Cartilage, 2010. **18**(11): p. 1402-1407.

21. Miriam A, B., Phillip F.J. Tirman, Charles G. Peterfy, Monte Zarlingo, John F. Feller, Frederic W. Bost, John P. Belzer, Thorsten K. Wischer, Harry K. Genant, *Accuracy of T2-weighted fast spin-echo MR imaging wIth fat saturation in detecting cartilage defects in the knee: comparison with arthroscopy in 130 patients.* . AJR American journal of roentgenology 1999. **172(4)**: p. 1073-80.

22. Hovis, K.K., et al., *Physical Activity Is Associated With Magnetic Resonance Imaging-Based Knee Cartilage T2 Measurements in Asymptomatic Subjects With and Those Without Osteoarthritis Risk Factors.* Arthritis and Rheumatism, 2011. **63**(8): p. 2248-2256.

23. Mosher, T.J., B.J. Dardzinski, and M.B. Smith, *Human articular cartilage: Influence of aging and early symptomatic degeneration on the spatial variation of T2 - Preliminary findings at 3 T.* Radiology, 2000. **214**(1): p. 259-266.

24. Li, X., et al., *In vivo T-1 rho arid T-2 mapping of articular cartilage in osteoarthritis of the knee using 3 T MRI.* Osteoarthritis and Cartilage, 2007. **15**(7): p. 789-797.

25. Owman, H., et al., *Association between findings on delayed gadolinium-enhanced magnetic resonance imaging of cartilage and future knee osteoarthritis.* Arthritis and Rheumatism, 2008. **58**(6): p. 1727-1730.

26. Bashir, A., et al., *Nondestructive imaging of human cartilage glycosaminoglycan concentration by MRI.* Magnetic Resonance in Medicine, 1999. **41**(5): p. 857-865.

27. Williams, A., et al., *Delayed gadolinium-enhanced magnetic resonance imaging of cartilage in knee osteoarthritis - Findings at different radiographic stages of disease and relationship to malalignment.* Arthritis and Rheumatism, 2005. **52**(11): p. 3528-3535.

28. Novakofski, K.D., et al., *High-Resolution Methods for Diagnosing Cartilage Damage In Vivo.* Cartilage, 2016. **7**(1): p. 39-51.

29. Favero, M., et al., *Early knee osteoarthritis.* RMD Open, 2015. **1**(Suppl 1): p. e000062.

30. Kennedy BF, K.K., Sampson DD, *A review of optical coherence elastography: fundamentals, techniques and prospects.* IEEE J Sel Quan Elec, 2014. **20(2)**(7101217).

31. Kennedy, K.M., et al., *Quantitative micro-elastography: imaging of tissue elasticity using compression optical coherence elastography.* Sci Rep, 2015. **5**: p. 15538.

32. Yun, S., et al., *High-speed spectral-domain optical coherence tomography at 1.3 mum wavelength.* Opt Express, 2003. **11**(26): p. 3598-604.

33. Park, B., et al., *Real-time fiber-based multi-functional spectral-domain optical coherence tomography at 1.3 microm.* Opt Express, 2005. **13**(11): p. 3931-44.

34. Wang, S. and K.V. Larin, *Optical coherence elastography for tissue characterization: a review.* J Biophotonics, 2015. **8**(4): p. 279-302.

35. Schmitt, J., *OCT elastography: imaging microscopic deformation and strain of tissue.* Opt Express, 1998. **3**(6): p. 199-211.

36. Nebelung, S., et al., *Towards Optical Coherence Tomography-based elastographic evaluation of human cartilage.* J Mech Behav Biomed Mater, 2016. **56**: p. 106-19.

37. Maroudas, A.I., *Balance between swelling pressure and collagen tension in normal and degenerate cartilage.* Nature, 1976. **260**(5554): p. 808-9.

38. Schlegel, P.N., *Testicular sperm extraction: microdissection improves sperm yield with minimal tissue excision.* Hum Reprod, 1999. **14**(1): p. 131-5.

39. Bernie, A.M., et al., *Comparison of microdissection testicular sperm extraction, conventional testicular sperm extraction, and testicular sperm aspiration for nonobstructive azoospermia: a systematic review and meta-analysis.* Fertil Steril, 2015. **104**(5): p. 1099-103 e1-3.

40. Dabaja, A.A. and P.N. Schlegel, *Microdissection testicular sperm extraction: an update.* Asian J Androl, 2013. **15**(1): p. 35-9.

41. Davis, C. and W. Kuang, *Optical coherence tomography: a novel modality for scrotal imaging.* Can Urol Assoc J, 2009. **3**(4): p. 319-322.

42. Ramasamy, R., et al., *Full field optical coherence tomography can identify spermatogenesis in a rodent sertoli-cell only model.* J Pathol Inform, 2012. **3**: p. 4.

43. Lue, Y.H., et al., *Single Exposure to Heat Induces Stage-Specific Germ Cell Apoptosis in Rats: Role of Intratesticular Testosterone on Stage Specificity.* Endocrinology, 1999. **140**(4): p. 1709-1717.

44. Lue, Y., et al., *Testicular Heat Exposure Enhances the Suppression of Spermatogenesis by Testosterone in Rats: The "Two-Hit" Approach to Male Contraceptive Development.* Endocrinology, 2000. **141**(4): p. 1414-1424.

45. Vermeer, K.A., et al., *Depth-resolved model-based reconstruction of attenuation coefficients in optical coherence tomography.* Biomed Opt Express, 2013. **5**(1): p. 322-37.

46. Wang, Y., et al., *GPU accelerated real-time multi-functional spectral-domain optical coherence tomography system at 1300nm.* Optics Express, 2012. **20**(14): p. 14797-14813.

47. Ma, J.K., *Optical Coherence Tomography Elastography Techniques for the Early Detections of Osteoarthritis in Rat Articular Cartilage* in *Bioengineering* 2013, University of California, Riverside. p. 50.

48. Schmitt, J.M., S.H. Xiang, and K.M. Yung, *Speckle in optical coherence tomography.* J Biomed Opt, 1999. **4**(1): p. 95-105.

49. Bashkansky, M. and J. Reintjes, *Statistics and reduction of speckle in optical coherence tomography.* Opt Lett, 2000. **25**(8): p. 545-7.

50. Hans-Jurgen Butt, B.C., Michael Kappl, *Force measurements with the atomic force microscope: Technique, interpretation and applications.* Surface Science Reports 2005. **59 (2005)**: p. 1-152.

51. K.A. Ross, M.G.S., *Analysis of the elastic modulus of agar gel by indentation* Journal of Texture Studies 1999. **30**(1): p. 17-27.

52. Nam, J., et al., *Sequential alterations in catabolic and anabolic gene expression parallel pathological changes during progression of monoiodoacetate-induced arthritis.* PLoS One, 2011. **6**(9): p. e24320.

53. Nam, J., et al., *Transcriptome-wide gene regulation by gentle treadmill walking during the progression of monoiodoacetate-induced arthritis.* Arthritis Rheum, 2011. **63**(6): p. 1613-25.

54. Pritzker, K.P., et al., *Osteoarthritis cartilage histopathology: grading and staging.* Osteoarthritis Cartilage, 2006. **14**(1): p. 13-29.

55. Frisbie, D.D., C.E. Kawcak, and C.W. McIlwraith, *Evaluation of the effect of extracorporeal shock wave treatment on experimentally induced osteoarthritis in middle carpal joints of horses.* Am J Vet Res, 2009. **70**(4): p. 449-54.

56. Bader, D.L. and G.E. Kempson, *The short-term compressive properties of adult human articular cartilage.* Biomed Mater Eng, 1994. **4**(3): p. 245-56.

57. Alexander, P.G., et al., *An In Vivo Lapine Model for Impact-Induced Injury and Osteoarthritic Degeneration of Articular Cartilage.* Cartilage, 2012. **3**(4): p. 323-33.

58. Furman, B.D., et al., *Joint degeneration following closed intraarticular fracture in the mouse knee: a model of posttraumatic arthritis.* J Orthop Res, 2007. **25**(5): p. 578-92.

59. Newberry, W.N., C.D. Mackenzie, and R.C. Haut, *Blunt impact causes changes in bone and cartilage in a regularly exercised animal model.* J Orthop Res, 1998. **16**(3): p. 348-54.

60. D'Lima, D.D., et al., *Impact of mechanical trauma on matrix and cells.* Clin Orthop Relat Res, 2001(391 Suppl): p. S90-9.

61. Hee MR, H.D., Swanson EA, Fujimoto JG., *Polarization-sensitive low-coherence reflectometer for birefringence characterization and ranging.* J Opt Soc Am B, 1922. **9**(6): p. 903-8.

62. Patel, N.A., et al., *Monitoring osteoarthritis in the rat model using optical coherence tomography.* IEEE Trans Med Imaging, 2005. **24**(2): p. 155-9.

63. Chu, C.R., et al., *Clinical diagnosis of potentially treatable early articular cartilage degeneration using optical coherence tomography.* J Biomed Opt, 2007. **12**(5): p. 051703.

64. de Boer, J.F., et al., *Two-dimensional birefringence imaging in biological tissue by polarization-sensitive optical coherence tomography.* Opt Lett, 1997. **22**(12): p. 934-6.

65. Jiao, S., G. Yao, and L.V. Wang, *Depth-resolved two-dimensional stokes vectors of backscattered light and mueller matrices of biological tissue measured with optical coherence tomography.* Appl Opt, 2000. **39**(34): p. 6318-24.

66. Park, B.H., et al., *In vivo burn depth determination by high-speed fiber-based polarization sensitive optical coherence tomography.* J Biomed Opt, 2001. **6**(4): p. 474-9.

67. Park, B.H., et al., *Jones matrix analysis for a polarization-sensitive optical coherence tomography system using fiber-optic components.* Opt Lett, 2004. **29**(21): p. 2512-4.

68. Drexler, W., et al., *Correlation of collagen organization with polarization sensitive imaging of in vitro cartilage: implications for osteoarthritis.* J Rheumatol, 2001. **28**(6): p. 1311-8.

69. Kasaragod, D.K., et al., *Experimental validation of an extended Jones matrix calculus model to study the 3D structural orientation of the collagen fibers in articular cartilage using polarization-sensitive optical coherence tomography.* Biomed Opt Express, 2012. **3**(3): p. 378-87.

70. Lee S-W, O.J.-T., Kim B-M, *Microscopic Imaging of Articular Cartilage using Polarization-Sensitive Optical Coherence Tomography.* Journal of Biomedical Engineering Research, 2005. **26**(1): p. 37-42.

71. Liu, B., C. Vercollone, and M.E. Brezinski, *Towards improved collagen assessment: polarization-sensitive optical coherence tomography with tailored reference arm polarization.* Int J Biomed Imaging, 2012. **2012**: p. 892680.

72. Mansfield, J.C., et al., *Collagen fiber arrangement in normal and diseased cartilage studied by polarization sensitive nonlinear microscopy.* J Biomed Opt, 2008. **13**(4): p. 044020.

73. SJ, M., *A review of some recent developments in polarization-sensitive optical imaging techniques for the study of articular cartilage.* Journal of Applied Physics, 2008. **105**(10): p. 102041.

74. Matcher, S.J., *What can biophotonics tell us about the 3D microstructure of articular cartilage?* Quant Imaging Med Surg, 2015. **5**(1): p. 143-58.

75. Shyu J-J, C.C.-H., Hsiung M-W, Yang P-N, Chen H-W, Kuo W-C, *Diagnosis of articular cartilage damage by polarization sensitive optical coherence tomography and the extracted optical properties.* Progress In Electromagnetics Research, 2009. **91**: p. 365-76.

76. Xie T, G.S., Zhang J, Chen Z, Peavy GM, *Use of polarization-sensitive optical coherence tomography to determine the directional polarization sensitivity of articular cartilage and meniscus.* Journal of biomedical optics, 2006. **11**(6): p. 064001--8.

77. Xie, T., et al., *Topographical variations in the polarization sensitivity of articular cartilage as determined by polarization-sensitive optical coherence tomography and polarized light microscopy.* J Biomed Opt, 2008. **13**(5): p. 054034.

78. JF, d.B., *Spectral/Fourier Domain Optical Coherence Tomography.* In: Drexler W. Fujimoto J, editors. Optical Coherence Tomography: Springer Berlin Heidelberg; , 2008: p. 147-75.

79. Park, B.H., et al., *Optic axis determination accuracy for fiber-based polarization-sensitive optical coherence tomography.* Opt Lett, 2005. **30**(19): p. 2587-9.

80. de Boer, J.F., T.E. Milner, and J.S. Nelson, *Determination of the depth-resolved Stokes parameters of light backscattered from turbid media by use of polarization-sensitive optical coherence tomography.* Opt Lett, 1999. **24**(5): p. 300-2.

81. BH, P., *Fiber-based polarization-sensitive optical coherence tomography* 2005, University of California, Irvine

82. Desrochers, J., M.W. Amrein, and J.R. Matyas, *Viscoelasticity of the articular cartilage surface in early osteoarthritis.* Osteoarthritis Cartilage, 2012. **20**(5): p. 413-21.

83. Huo, L., et al., *Forward-viewing resonant fiber-optic scanning endoscope of appropriate scanning speed for 3D OCT imaging.* Opt Express, 2010. **18**(14): p. 14375-84.

84. Munce, N.R., et al., *Electrostatic forward-viewing scanning probe for Doppler optical coherence tomography using a dissipative polymer catheter.* Opt Lett, 2008. **33**(7): p. 657-9.

85. Fujimoto, J.G., et al., *Optical coherence tomography: an emerging technology for biomedical imaging and optical biopsy.* Neoplasia, 2000. **2**(1-2): p. 9-25.

86. Tearney, G.J., et al., *In vivo endoscopic optical biopsy with optical coherence tomography.* Science, 1997. **276**(5321): p. 2037-9.

87. Pierce, M., et al., *Effects of sample arm motion in endoscopic polarization-sensitive optical coherence tomography.* Opt Express, 2005. **13**(15): p. 5739-49.

88. Liang, C.P., et al., *A forward-imaging needle-type OCT probe for image guided stereotactic procedures.* Opt Express, 2011. **19**(27): p. 26283-94.

89. Wu, J., et al., *Paired-angle-rotation scanning optical coherence tomography forward-imaging probe.* Opt Lett, 2006. **31**(9): p. 1265-7.

90. Iftimia, N.V., et al., *Spectral-domain low coherence interferometry/optical coherence tomography system for fine needle breast biopsy guidance.* Rev Sci Instrum, 2009. **80**(2): p. 024302.

91. Edmonson, J.M., *History of the instruments for gastrointestinal endoscopy.* Gastrointest Endosc, 1991. **37**(2 Suppl): p. S27-56.

92. Tearney, G.J., et al., *Three-dimensional coronary artery microscopy by intracoronary optical frequency domain imaging.* JACC Cardiovasc Imaging, 2008. **1**(6): p. 752-61.

93. Bezerra, H.G., et al., *Intracoronary optical coherence tomography: a comprehensive review clinical and research applications.* JACC Cardiovasc Interv, 2009. **2**(11): p. 1035-46.

94. Yang, V.X., et al., *High speed, wide velocity dynamic range Doppler optical coherence tomography (Part III): in vivo endoscopic imaging of blood flow in the rat and human gastrointestinal tracts.* Opt Express, 2003. **11**(19): p. 2416-24.

95. Rollins, A.M., et al., *Real-time in vivo imaging of human gastrointestinal ultrastructure by use of endoscopic optical coherence tomography with a novel efficient interferometer design.* Opt Lett, 1999. **24**(19): p. 1358-60.

96. Krakowski C J, O.L.S., *Ultrasound-Guided Peripheral Nerve Block Anesthesia with Emphasis on the Interscalene Approach to Brachial Plexus Blockade.* Advancements and Breakthroughs in Ultrasound Imaging. Chapter 5., 2013: p. 119-136.

97. Pan, Y., et al., *Hand-held arthroscopic optical coherence tomography for in vivo high-resolution imaging of articular cartilage.* J Biomed Opt, 2003. **8**(4): p. 648-54.